

Interactions in Rare Earth Doped Nanoparticles: A Multi-Transition, Concentration, and Excitation Path Analysis

Pauline Perrin,^{*,†} Luiz Fernando Dos Santos,^{‡,†} Diana Serrano,[†] Alexey Tiranov,[†]
Jocelyn Achard,[¶] Alexandre Tallaire,[†] Rogéria R. Gonçalves,[‡] and Philippe
Goldner^{*,†}

[†]*Chimie ParisTech, PSL University, CNRS, Institut de Recherche de Chimie Paris, 75005
Paris, France*

[‡]*Laboratorio de Materiais Luminescentes Micro e Nanoestruturados – Mater Lumen,
Departamento de Química, Faculdade de Filosofia, Ciências e Letras de Ribeirão Preto,
Universidade de São Paulo, Ribeirão Preto, SP, Brazil*

[¶]*LSPM, CNRS, Université Sorbonne Paris Nord, 99 avenue JB Clement, 93460
Villetaneuse, France*

E-mail: pauline.perrin@chimieparistech.psl.eu; philippe.goldner@chimieparistech.psl.eu

Abstract

Understanding and modeling energy transfer mechanisms in rare-earth-doped nano-materials is essential for advancing luminescent technologies used in bioimaging, optical thermometry, and solid-state lasers. In this work, we investigate the photoluminescence dynamics of Yb^{3+} and Er^{3+} ions in Y_2O_3 nanoparticles over a wide concentration range (0.5–17%), using both direct and upconversion excitation. Luminescence decays

of green, red, and near-infrared transitions were measured and analyzed using a rate-equation model incorporating radiative and non-radiative processes, energy transfer mechanisms, and defect-related quenching. The model successfully reproduces experimental trends across most concentrations and excitation paths. This work provides a reliable and predictive framework for modeling energy transfer in rare-earth doped materials and offers valuable insights for optimizing photoluminescent properties in nanostructured systems.

Introduction

Energy transfer phenomena in rare-earth doped materials have been investigated for a long time and remain a major topic in solid-state luminescence on both theoretical aspects and applications.¹⁻³ Among many excitation/emission schemes, those enabling emission following excitation at longer wavelengths are of particular interest. They rely on energy transfers between excited states with long enough lifetimes. As the number of successive energy transfers increases, so does the energy of the populated levels. The so-called energy transfer up-conversion (ETU)⁴⁻⁷ and closely related phenomena such as avalanche up-conversion,⁸ finds applications in many fields such as lasers,⁹ thermometry,¹⁰ bioimaging,¹¹ or super-resolution fluorescence microscopy.¹²

A key point in material development for efficient ETU is the ability to accurately model energy transfers in addition to the properties of isolated (non-interacting) ions. This is complex since ETU typically involve several rare earth ions, and thus multiple energy levels and a large number of possible energy transfers. Energy transfers are also strongly dependent on the distance between ions,¹³ which means that modeling the large ensembles of ions experimentally observed will need careful averaging over ions' spatial distribution. These questions have motivated many studies, from obtaining explicit equations for the ions decay dynamics^{2,14,15} to heavy numerical computations,¹⁶ through semi-phenomenological rate equation approaches.^{5,17}

The latter typically involve many parameters corresponding to the ions and levels involved, which have to be determined from the levels' decay rates and/or luminescence intensities. As these parameters are likely to be combined in complex ways in the decays of virtually all levels, they are difficult to evaluate from small series of measurements of a few levels and rare earth concentrations. This can make the validity of reported parameters over e.g. a broad range of dopant concentrations or excitation wavelengths, as well as their physical meaning, difficult to assess. In addition, new phenomena become important for nanostructured materials^{18,19} which are at the heart of key applications, like bio-imaging or thermometry.⁷ It is for example well documented that in nanoparticles or thin films, defects capable of quenching luminescence are more prominent than in their bulk counterparts and are often located at free surfaces or interfaces.²⁰⁻²² This results in further complexity in theoretical and modeling studies, especially since these defects can not always be clearly identified and/or controlled.

In this work, we present a comprehensive study of the Er^{3+} , Yb^{3+} system in Y_2O_3 nanoparticles. Y_2O_3 is among the oxide crystals with the lowest phonon cut-off frequency which reduces non-radiative relaxations and levels with longer lifetimes.²³ Y_2O_3 is a versatile host that can be synthesized under the forms of high-quality single bulk crystals,²⁴ transparent ceramics^{25,26}, thin films,²⁷ and nanoparticles.²⁸⁻³⁰ It finds applications in lasers,³¹ luminescent probes and sensors,^{32,33} and, more recently, as a promising platform for optical quantum technologies.³⁴⁻³⁶ All of them rely on or have to consider energy transfer phenomena.

Our study is based on the decay times of the main transitions located between from 0.52 to 1.5 μm that have been measured as a function of Er^{3+} and Yb^{3+} concentrations and in singly- and co-doped samples. This was performed under direct excitation of the probed levels as well under 0.98 μm excitation in Yb^{3+} , Er^{3+} -co-doped samples to investigate ETU process. Such an extensive approach has never been reported to our knowledge.

Using a rate equation modeling, these data allowed us to independently extract energy

transfer rates for different transitions, doping levels, and excitations wavelengths. Luminescence quenching by defects was also observed and included in the models. This enables reproducing and predicting Er^{3+} and Yb^{3+} decay times for most concentrations in singly- as well as co-doped samples and for emission excited directly or through ETU, indicating that a description in terms of populations averaged over all excited ions is adequate. Moreover, the analysis highlights a doping regime that likely optimizes ETU efficiency. These results open the way to accurate modeling and prediction of the dynamics of RE energy level populations in complex situations. In contrast to simulations based on microscopic configurations, the rate equation modeling involves small to moderate computing power and allows for easier physical interpretation for fast, reliable, and efficient material development.

Methodology

To identify the dominant interactions between ions, we first analyze those occurring within the same species—Yb–Yb and Er–Er—before turning to Er–Yb interactions. This is achieved by examining how excited-state lifetimes, or equivalently relaxation rates, vary with dopant concentration.

Our approach combines a qualitative analysis, aimed at identifying the most likely interaction pathways for each energy level, with a quantitative analysis based on extracting relaxation rates associated with each process. This is done by modeling population dynamics using rate equations.

Rate equations can be used when all probed ions evolve similarly over time. as a function of time and can thus be accurately described by average populations for the different levels. This situation is observed for non-interacting ions, i.e. at low doping concentrations (typically $\leq 0.1 - 0.5\%$). In the opposite situation of high doping concentrations ($\geq 5\%$), where fast migration of energy results in identical average populations for all ions, rate equations are also appropriate. In both cases, exponential decays are experimentally observed for

directly excited levels. In contrast, at intermediate concentrations, each ion is surrounded by other ions, or defects, located at varying positions. Inhomogeneous interactions lead to non-exponential decays which cannot be rigorously described by rate equations anymore.

In the following, we use rate equations across all concentrations to extract spatially averaged transfer rates, allowing for a simpler and consistent modeling approach. This avoids the complexity of spatially resolved models, while still providing useful physical insights.

Each excited-state population n_i based on radiative decay rates (taken from literature measured in a high quality ceramic²³), non-radiative decay rates (determined from low-concentration experiments or fitted), and energy transfer rates, which are iteratively refined throughout the study. Further details are provided in the Modeling section and in the SI.

Regarding the experimental work, time-resolved photoluminescence decays $I(t)$ of key energy levels were measured following direct excitation. For Yb-doped nanoparticles, luminescence from the $^2F_{5/2}$ level to the ground state was recorded, while for Er-doped nanoparticles, emissions from the $^4S_{3/2}$, $^4F_{9/2}$, $^4I_{11/2}$ and $^4I_{13/2}$ levels were measured.

We use $K_i = 1/\tau_i$ as a figure of merit to compare experimental data with modeling predictions. The characteristic time τ_i is estimated from both experimental data and the model as:

$$I_i(t_0 + 2\tau_i) = I_i(t_0)/e^2 \quad (1)$$

where t_0 the time of maximum intensity.

This method of estimating τ accounts for 86% of the luminescence decay, providing a trade-off between the short- and long-lived components of the most significant portion of the emitted intensity.

Modeling

We consider a system composed of Yb^{3+} ions (with a concentration N_{Yb}) with two energy levels, and Er^{3+} ions (with a concentration N_{Er}) limited to seven energy levels i , as presented

on Figure 1. The $^2\text{H}_{11/2}$ and $^4\text{S}_{3/2}$ levels are assumed to be in thermal equilibrium and are grouped into a single level.

In some studies on fluoride-based materials,^{37,38} high up-conversion efficiency has led to the observation of blue emissions originating from three-photon processes. Although such effects have also been reported in Y_2O_3 systems,³⁹ in our nanoparticles—excited at low excitation power—no signatures of three-photon processes were observed. This confirms that the observed emissions result solely from two-photon up-conversion, with no additional excited states involved.

To model ion interactions, we employ a system of rate equations describing the time evolution of the population density n_i of each excited-state level i , according to the relation dn_i/dt , as a function of the interaction rates k and the populations of other relevant energy levels.⁴⁰ This approach assumes rapid energy migration and relies on average decay rates across the system. The following processes are included in the model:

1. radiative decays $k_{\text{R}ij}$ from a level i to a level j
2. non-radiative decays $k_{\text{NR}i,i-1}$ from a level i to the level $i - 1$ caused by interactions with lattice phonons
3. energy transfer $\text{Yb} \rightarrow \text{Er}$ $k_{\text{ET}ij}$ populating a level j from a level i of Er^{3+} ions
4. back energy transfer (BT) $\text{Er} \rightarrow \text{Yb}$ $k_{\text{BT}ij}$ populating a level j from a level i of Er^{3+} ions
5. cross-relaxations (CR) $\text{Er} \rightarrow \text{Er}$ $k_{\text{CR}ij}$ depopulating the levels i and j of Er^{3+} ions
6. additional defect-related quenching path $k_{\text{ET}1'0'd}$ depopulating the Yb^{3+} excited state level
7. additional defect-related quenching paths observed for high doping concentrations ($> 5\%$) $k_{\text{HC}i}$ depopulating i level of Er^{3+} ions

As mentioned in the Methodology, radiative decay rates are taken from literature.^{23,41} Non-radiative decay rates are either determined from low-concentration experiments, fitted to experimental data, or estimated based on the energy gap. Some energy transfer rates—including BT and CR processes—are iteratively refined throughout the study. The remaining rates are fixed depending on whether the process is resonant or non-resonant (phonon-assisted).⁴²

The mechanisms taken into account for this modeling are represented on Figure 1. Further details are provided in the Supplementary Information.

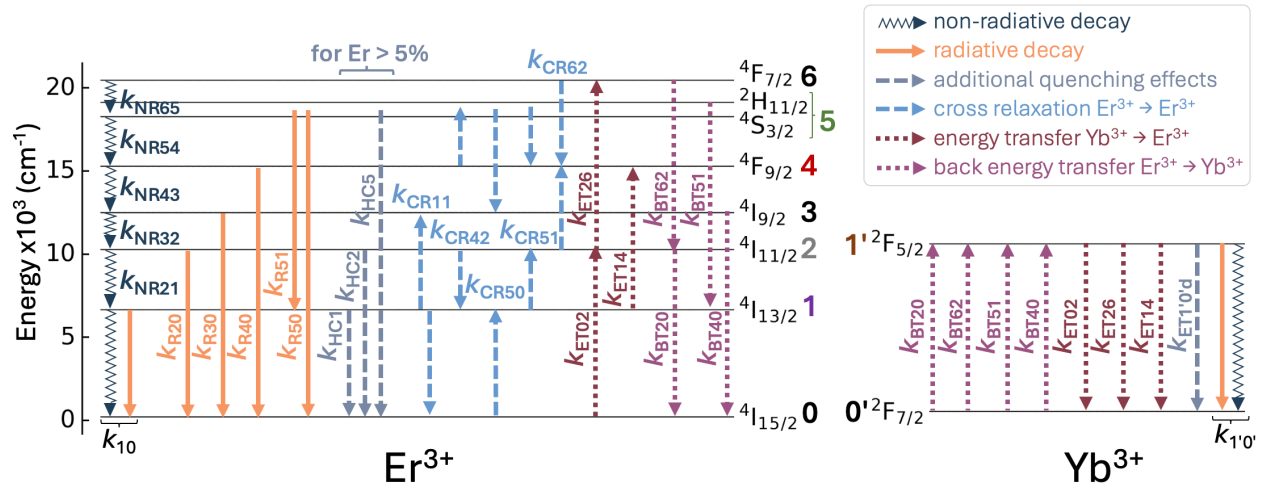


Figure 1: Energy level diagram of Yb^{3+} and Er^{3+} ions and illustration of the interactions considered in our modeling.

Experimental

Synthesis of Yb^{3+} and Er^{3+} doped Y_2O_3 nanoparticles

Crystalline Y_2O_3 -based nanoparticles doped with Yb^{3+} and Er^{3+} ions were successfully synthesized through a homogeneous precipitation route followed by carefully controlled thermal treatments.^{43,44} In brief, $\text{Y}(\text{OH})\text{CO}_3 \cdot n\text{H}_2\text{O}$ was employed as the precursor material. The homogeneous precipitation was induced via the thermolysis of urea in an aqueous medium containing $\text{Y}(\text{NO}_3)_3 \cdot 6\text{H}_2\text{O}$ (99.99% purity, Alfa Aesar®) and urea (99% purity, Sigma-

Aldrich®), at final concentrations of 7.5 mmol·L⁻¹ and 3 mol·L⁻¹, respectively. The dopant ions Er³⁺ and Yb³⁺ were introduced via their respective nitrate salts, Er(NO₃)₃·6H₂O and Yb(NO₃)₃·5H₂O, with purities of 99.99% and 99.9999% (Alfa Aesar®).

A total of ten samples were prepared with varying dopant concentrations. For Er³⁺-doped nanoparticles, the molar doping relative to Y³⁺ were 0.5%, 2%, 7%, and 17%. In the case of Yb³⁺ doping, the compositions included 0.5%, 1%, 2%, 5%, 9%, and 17% molar ratios with respect to Y³⁺ molar amount.

Further details about the synthesis are provided in Supplementary Information.

Pulsed optical parametric oscillator

For PL spectra and decays, Yb³⁺ and Er³⁺ ions were excited by 6 ns long pulses from a tunable (linewidth <5 cm⁻¹) optical parametric oscillator (OPO) pumped by a Nd:YAG Q-switched laser (Ekspla NT342B-SH). Visible fluorescence was collected and detected through a spectrometer (Acton SP2300) equipped with three different gratings and an intensified charge-coupled device (ICCD) camera (Princeton Instruments PI-MAX4) for spectra or a photo-multiplier tube (S20 cathode) for decays. NIR spectra and decays were measured with an InGaAs photodiode detector (FEMTO OE-200).

Results and discussion

Morphology and emission spectra

Nanoparticles morphology was investigated using Scanning Electron Microscopy (SEM). Figure 2.C shows SEM images of nanoparticles doped with 0.5% Yb, confirming their spherical morphology and approximate size of 100 nm. This synthesis procedure leads to single-crystalline nanoparticles in Y₂O₃ cubic phase (I-3a) with limited aggregation.²⁸ Yb³⁺ and Er³⁺ ions substitute Y³⁺ ions at both C₂ (24-fold multiplicity) and C_{3i} (8-fold multiplicity) crystallographic sites in the Y₂O₃ lattice. Due to the presence of an inversion center at C_{3i}

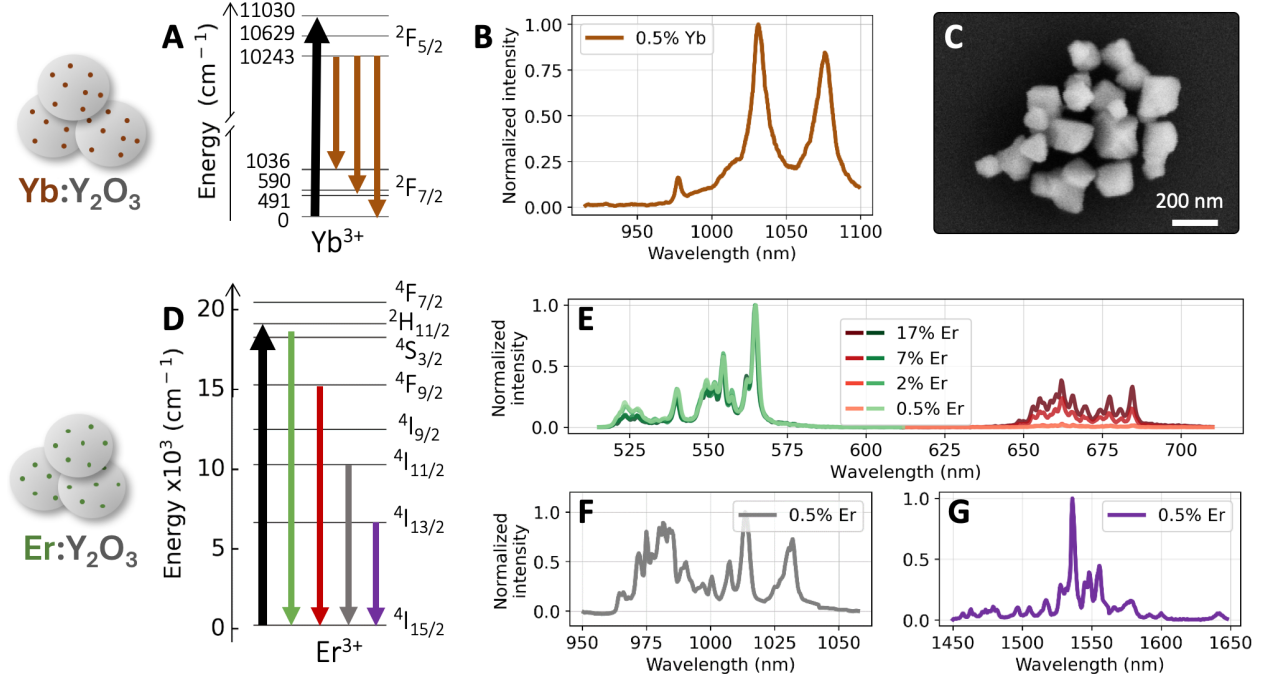


Figure 2: **Singly-doped nanoparticles - Emission spectra and morphology.** (A) Energy level diagram of Yb^{3+} , highlighting the three main emission transitions corresponding to peaks at 977 nm, 1030 nm, and 1075 nm. (B) Emission spectra of nanoparticles doped with 0.5% Yb, showing the emission lines between the Stark levels associated with the transitions in (A). (C) SEM image of nanoparticles doped with 0.5% Yb, revealing a spherical morphology and an average diameter of approximately 100 nm. (D) Energy level diagram of Er^{3+} . (E) Emission spectra in the visible range following excitation at 520 nm (indicated by the black arrow), normalized to the green emission peak. A decrease in the red-to-green emission ratio is observed with increasing Er^{3+} doping concentration. (F,G) Emission spectra in the near-infrared (1 μm) range (corresponding to the $4I_{11/2} \rightarrow 4I_{15/2}$ transition) and around 1.5 μm (corresponding to the $4I_{13/2} \rightarrow 4I_{15/2}$ transition) of nanoparticles doped with 0.5% Er^{3+} excited at 520 nm.

sites, electric dipole (ED) transitions are forbidden for ions occupying these positions.⁴⁵ However, magnetic dipole (MD) transitions, governed by the selection rule $\Delta J = 0, \pm 1$, remain allowed and can exhibit non-zero intensity. As a result, only the $2F_{5/2} \rightarrow 2F_{7/2}$ transition of Yb^{3+} ions and the $4I_{13/2} \rightarrow 4I_{15/2}$ transition of Er^{3+} ions are observed from C_{3i} sites. Thus, most of the emissions analyzed in this study originate from transitions of ions located at C_2 sites.

To evaluate the luminescent properties of the rare-earth ions, emission spectra of Yb-doped nanoparticles were recorded at room-temperature, by exciting the $4F_{7/2} \rightarrow 4F_{5/2}$

transition at 905 nm. The near-infrared (NIR) emission spectrum presented on Figure 2.B, displays three main peaks at 977 nm, 1030 nm and 1075 nm, attributed to transitions between the Stark levels of $^2F_{5/2}$ and $^2F_{7/2}$ manifolds, as shown in Figure 2.A.^{46,47} Moreover, the recorded spectra are consistent with those expected for Y_2O_3 , confirming the good crystallization of the material. No significant spectral variations are observed across the different Yb^{3+} doping concentrations.

The NIR emission spectra of Er^{3+} doped nanoparticles are presented in Figure 2.F and Figure 2.G, after exciting the $^4I_{15/2} \rightarrow ^2H_{11/2}$ transition at 520 nm. Emission around 1 μm is attributed to the $^4I_{11/2} \rightarrow ^4I_{15/2}$ transition, while the emission around 1.5 μm corresponds to the $^4I_{13/2} \rightarrow ^4I_{15/2}$ transition.^{26,48} Finally, the visible emission spectra of Er-doped nanoparticles, following excitation at 520 nm, are shown in Figure 2.E. The green emission around 550 nm is attributed to relaxation from the thermally coupled $^2H_{11/2}$ and $^4S_{3/2}$ levels to the ground state. On the other hand, the red emission around 660 nm arises from the $^4F_{9/2} \rightarrow ^4I_{15/2}$ transition. An increase in red emission relative to green emission is observed with increasing Er^{3+} concentration, as previously reported.⁴⁹ This enhancement is attributed to cross-relaxation mechanisms, which result in populating more efficiently the $^4F_{9/2}$ level at higher concentrations. A more detailed discussion of these mechanisms is provided later.

Singly-doped nanoparticles

To gain both qualitative and quantitative insight into the mechanisms occurring between ions of the same species— Yb^{3+} - Yb^{3+} and Er^{3+} - Er^{3+} — such as non-radiative decays, cross-relaxations (CR) and additional defect-related quenching, we first investigated singly doped nanoparticles. Photoluminescence decays $I(t)$ of key energy levels were thus measured under direct excitation and are presented in Figure 3. Table 1 (resp. Table 2) summarizes up experimental lifetimes obtained in Yb- (resp. Er-) doped nanoparticles.

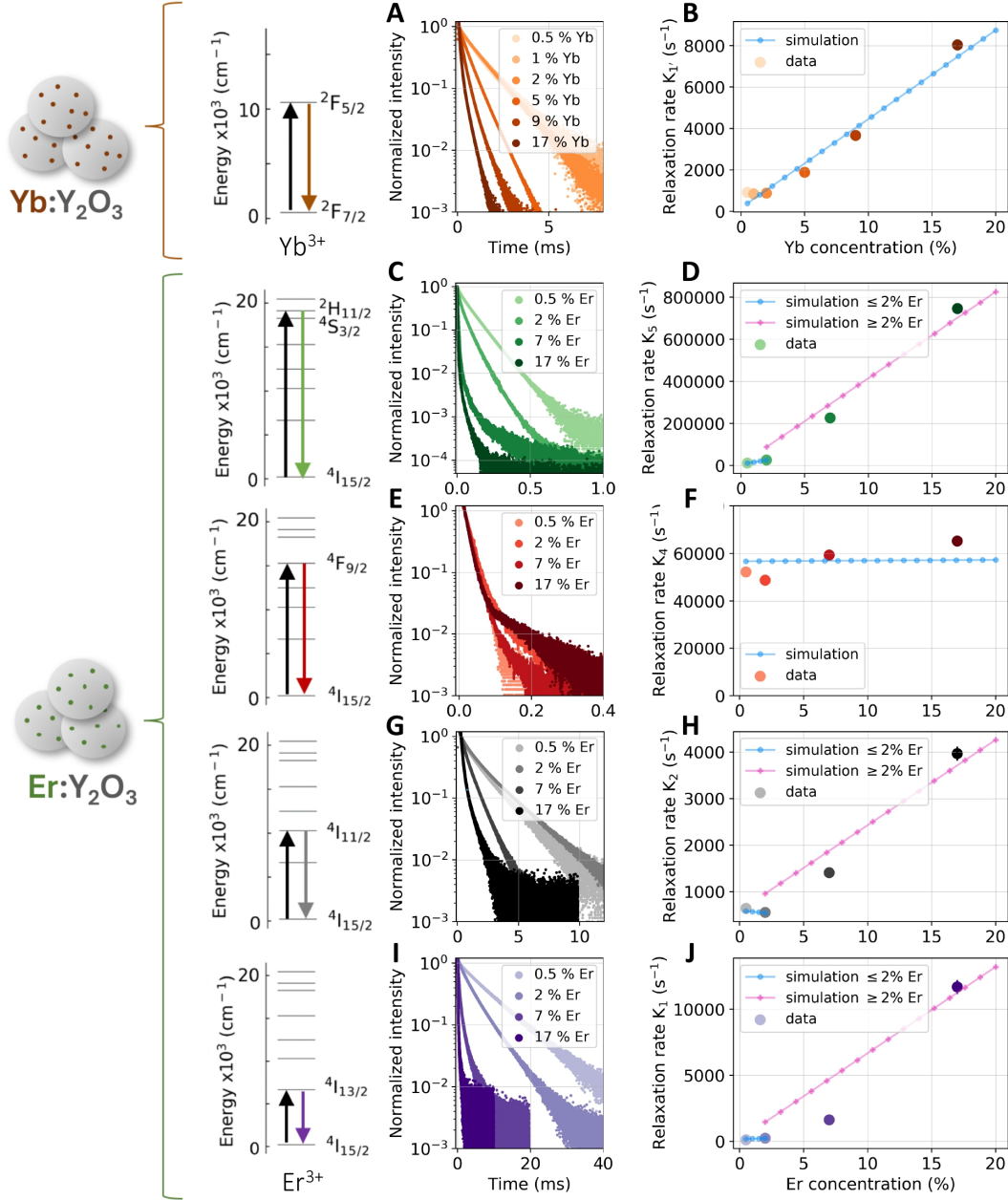


Figure 3: **Singly-doped nanoparticles - under direct excitation.** (A) Luminescence decay of Yb³⁺ excited state level for various doping levels and (B) variation of the relaxation rate K_1 , as a function of Yb³⁺ concentration. (C) Luminescence decay of Er³⁺ from the green-emitting levels ²H_{11/2}, ⁴S_{3/2} → ⁴I_{15/2} and (D) variation of the relaxation rate K_5 as a function of Er³⁺ concentration. (E) Luminescence decay of Er³⁺ red-emitting level ⁴F_{9/2} → ⁴I_{15/2} and (F) variation of the relaxation rate K_4 as a function of Er³⁺ concentration. (G) Luminescence decay of Er³⁺ around 1 μ m ⁴I_{11/2} → ⁴I_{15/2} and (H) variation of the relaxation rate K_2 as a function of Er³⁺ concentration. (I) Luminescence decay of Er³⁺ around 1.5 μ m ⁴I_{13/2} → ⁴I_{15/2} and (J) variation of the relaxation rate K_1 as a function of Er³⁺ concentration.

Table 1: Yb^{3+} excited state lifetimes (ms) measured for different doping concentrations in the singly-doped nanoparticles, and compared with the one reported for a ceramic sample.⁵⁰

	Yb concentration						
	<i>nanoparticles</i>						<i>ceramic</i> ⁵⁰
<i>level</i>	0.5 %	1 %	2 %	5 %	9 %	17 %	1 %
² F _{5/2}	1.1	1.2	1.1	0.53	0.27	0.12	0.91

Table 2: Er^{3+} lifetimes (ms) of different energy levels for various doping concentrations of the singly-doped nanoparticles, and compared to values reported for a ceramic sample.²³

<i>level</i>	Er concentration				
	<i>nanoparticles</i>				<i>ceramic</i> ²³
	0.5 %	2 %	7 %	17 %	0.5 %
² H _{11/2} , ⁴ S _{3/2}	0.085	0.038	0.004	0.001	0.088
⁴ F _{9/2}	0.019	0.021	0.017	0.015	0.030
⁴ I _{11/2}	1.56	1.80	0.71	0.25	3.9
⁴ I _{13/2}	8.1	4.0	0.6	0.09	8.0

Yb^{3+} doped nanoparticles

Figure 3.A presents Yb^{3+} luminescence decay curves following pulsed excitation at 905 nm. At low concentration (up to 2%), the $^2\text{F}_{5/2}$ lifetime τ remains around 1 ms consistent with previous studies in ceramics, confirming the high crystalline quality of the nanoparticles.^{50,51} For higher doped nanoparticles (5%, 9% and 17%), the decay accelerates significantly, with τ decreasing to approximately 0.12 ms at the highest Yb^{3+} concentration. This trend suggests an increased probability of relaxation through non-radiative mechanisms, likely driven by energy diffusion among Yb^{3+} ions, followed by energy transfer to centers that relax non-radiatively.⁵²

Furthermore, for this range of high concentrations, the fluorescence decay does not follow a purely mono-exponential function over time. Instead, an initial rapid intensity drop is observed, which then transitions into a mono-exponential behavior. This characteristic trend is indicative of a distribution of energy transfers Yb^{3+} to defects, arising from variations in the local environment of individual donors. As a result, the interaction strengths among Yb^{3+} ions differ, leading to a distribution of lifetimes.^{1,53} The experimental decay curves

$I(t)$ are well-fitted using the model developed by Inokuti and Hirayama for dipole-dipole interactions between donors and acceptors, with an interaction parameter of $s = 6^{15}$ (Figure S6).

Figure 3.B presents the relaxation rate $K_{1'}$, estimated using Equation 1, as a function of Yb^{3+} concentration. We observe two regimes: at low concentrations up to 2%, $K_{1'}$ is nearly constant and from 5% it increases linearly.

The first regime is attributed to limited energy migration, where only Yb^{3+} ions in close proximity to defects undergo quenching. In the second regime, as Yb^{3+} concentration increases, a larger fraction of Yb^{3+} ions are situated near defects, due to increased energy migration, leading to enhanced quenching. This manifests by a rapid initial decay followed by an exponential tail. This exponential component can be described by an additional relaxation term of the form $k = CN_A N_D$, where N_A represents the concentration of acceptors (i.e., defects), N_D corresponds to the concentration of donors (i.e., Yb^{3+} ions), and C is a parameter accounting for both diffusion among the donors and energy transfer to the acceptors.¹ The observed linear dependence suggests that the defect concentration remains constant across the studied range. In the following, we note $k_{\text{ET}1'0'd}$ the energy transfer rate from Yb^{3+} ions to defects where $k_{\text{ET}1'0'd} = CN_A$, to incorporate this concentration quenching into the modeling.

Consequently, we express the relaxation rate $K_{1'}$ of the Yb^{3+} excited state as $K_{1'} = k_{1'0'} + k_{\text{ET}1'0'd} n_{0'}$, where $k_{1'0'}$ accounts for both radiative and non-radiative decay rates, and $n_{0'} \approx N_{\text{Yb}}$ assuming low excitation power. This approach enables accurate modeling across a broad concentration range. A linear fit of $K_{1'} = f(N_{\text{Yb}})$ leads to $k_{1'0'} = 173 \text{ s}^{-1}$ and $k_{\text{ET}1'0'd} = 2.2 \times 10^{-18} \text{ cm}^3.\text{s}^{-1}$. The relaxation rate values, obtained from the simulation over a wide concentration range, are plotted in blue in Figure 3.B. These values exhibit good agreement with the experimental data in the concentration range of 2 to 17%, which is the primary focus of this study. The relaxation rate is slightly underestimated in the 0.5 to 1% range; however, this lower concentration range is not relevant to the scope of our work.

In summary, the analysis reveals a clear trend of increased luminescence decay with higher Yb^{3+} concentration, particularly due to energy transfer to defects. By adding and adjusting the energy transfer rate $k_{\text{ET1}'0'\text{d}}$, the model developed effectively describes these interactions.

Er³⁺ doped nanoparticles

Er³⁺ ions possess a rich energy level structure with multiple excited states involved in energy transfer and relaxation processes. To identify the dominant interactions contributing to ETU, we focus on four key levels that play central roles in the emission dynamics: ²H_{11/2}, ⁴S_{3/2} (green emission), ⁴F_{9/2} (red emission), ⁴I_{11/2} (1 μ m emission), ⁴I_{13/2} (1.5 μ m emission).

Green emission. Figure 3.C shows the luminescence decay curves corresponding to transitions from the thermalized ²H_{11/2} and ⁴S_{3/2} levels to the ground state in nanoparticles doped with 0.5%, 2%, 7%, and 17% of Er³⁺.

The lifetime of the green-emitting levels in nanoparticles doped with 0.5% Er³⁺ is estimated to be 85 μ s. This value is consistent with those reported for high-quality reference materials, such as 88 μ s in ceramics containing 0.2% Er³⁺,²³ and approximately 100 μ s in high-quality polycrystalline thin films with Er³⁺ concentrations below 1%.⁵⁴ The luminescence decay curves deviate from a mono-exponential trend, likely due to inhomogeneities in energy transfer probabilities, similar to what is observed for Yb³⁺ ions. Moreover, the decays reveal a pronounced decrease in lifetime with increasing Er³⁺ concentration. This effect is attributed to the cross-relaxation process CR50 (²H_{11/2}, ⁴I_{15/2}) \rightarrow (⁴I_{9/2}, ⁴I_{13/2}).^{40,54} This non-resonant process characterized by an energy mismatch of $\Delta E = 185 \text{ cm}^{-1}$, is highly efficient due to 1) its involvement of the ground state, which remains predominantly populated, and 2) its energy gap being significantly smaller than the maximum phonon energy in the crystal ($\approx 550 \text{ cm}^{-1}$).

Figure 3.D illustrates the variation of the relaxation rate K_5 as a function of Er³⁺ concentration. CR50 mechanism contributes to the relaxation rate K_5 as $k_{\text{CR50}}n_0$, where k_{CR50} represents the associated energy transfer rate, and $n_0 \approx N_{\text{Er}}$ assuming low excitation power. Thus, if CR50 interaction was the dominant contributor, K_5 would exhibit a linear dependence on the dopant concentration. However, deviations from this trend at high doping levels indicate the presence of additional quenching mechanisms, likely related to surface defects. To account for this, we distinguish between two regimes in our modeling.

For low Er^{3+} concentrations ($\leq 2\%$), the relaxation rate is well described by a linear model: $K_5 = k_{\text{R50}} + k_{\text{R51}} + k_{\text{NR54}} + k_{\text{CR50}}n_0$. In this regime, a linear fit—with the radiative rates k_{R50} and k_{R51} fixed (see Supplementary Information)—leads to $k_{\text{NR54}} = 5.5 \times 10^3 \text{ s}^{-1}$ and $k_{\text{CR50}} = 4.9 \times 10^{-17} \text{ cm}^3.\text{s}^{-1}$.

At higher Er^{3+} concentrations ($\geq 2\%$), an additional quenching term $k_{5\text{HC}}$ is introduced to account for enhanced quenching effects. The modified expression becomes: $K_5 = k_{\text{R50}} + k_{\text{R51}} + k_{\text{NR54}} + k_{\text{CR50}}n_0 + k_{5\text{HC}}n_0$. Fitting the data with only $k_{5\text{HC}}$ as a free parameter, gives $k_{5\text{HC}} = 1.6 \times 10^{-16} \text{ cm}^3.\text{s}^{-1}$.

The relaxation rates extracted from simulations—plotted in blue for the low-concentration regime and in pink for the high-concentration case in Figure 3.D, show good agreement with experimental data.

Red emission. Figure 3.E presents the luminescence decay curves from the red-emitting level corresponding to the transition $^4\text{F}_{9/2} \rightarrow ^4\text{I}_{15/2}$ in nanoparticles doped with different concentrations of Er^{3+} .

The luminescence decays exhibit a nearly mono-exponential behavior and remain largely unaffected by increasing dopant concentration. As shown in Figure 3.F, the relaxation rate K_4 varies between $4.9 \times 10^4 \text{ s}^{-1}$ and $6.5 \times 10^4 \text{ s}^{-1}$. This high relaxation rate is primarily attributed to the small energy gap to the adjacent $^4\text{I}_{9/2}$ level, which enables an efficient multiphonon relaxation pathway.

A linear fit of $K_4 = k_{\text{R40}} + k_{\text{NR43}}$ leads to $k_{\text{NR43}} = 5.5 \times 10^4 \text{ s}^{-1}$, with k_{R40} fixed to a literature value. The relaxation rates estimated from the simulation, plotted in blue in Figure 3.F, are close to the experimental data.

Red-to-green ratio. The increase in the red-to-green (R/G) ratio with Er^{3+} concentration can be attributed to the role of the CR50 process, which populates the $^4\text{I}_{9/2}$ and $^4\text{I}_{13/2}$ levels. The $^4\text{I}_{9/2}$ level feeds efficiently to $^4\text{I}_{11/2}$ via multiphonon relaxation due to the relatively small energy gap ($\approx 2215 \text{ cm}^{-1}$). Consequently, the ETU process ($^4\text{I}_{11/2}, ^4\text{I}_{13/2} \rightarrow ^4\text{F}_{9/2}, ^4\text{I}_{15/2}$) becomes more efficient at higher Er^{3+} concentrations, leading to the observed

increase in the R/G ratio.

Long time-scale component in visible decays induced by energy transfer from NIR levels.

For highly doped nanoparticles, a rapid initial luminescence decay is followed by a slower decay component in the green-emitting levels ($N_{\text{Er}} > 7\%$, after approximately 150 μs) and red-emitting levels ($N_{\text{Er}} > 2\%$, after approximately 0.1 ms), characteristic of an ET process.²⁹ The slower decay in the green-emitting levels results from a $(^4\text{I}_{11/2}, ^4\text{I}_{11/2}) \rightarrow (^4\text{F}_{7/2}, ^4\text{I}_{15/2})$ process. The $^4\text{I}_{11/2}$ level is populated via multiphonon relaxations, following a cascade from the $^4\text{S}_{3/2}$ level to $^4\text{F}_{9/2}$, then to $^4\text{I}_{9/2}$, and finally to $^4\text{I}_{11/2}$. Once the $^4\text{F}_{7/2}$ level is populated via up conversion, the $^2\text{H}_{11/2}$ and $^4\text{S}_{3/2}$ levels are replenished through multiphonon relaxation. Given the extended lifetime of the $^4\text{I}_{11/2}$ level, it serves as a reservoir, feeding the green-emitting levels and resulting in the long-tail behavior observed in the fluorescence decay.

For the red-emitting level, the $^4\text{F}_{9/2}$ level is populated via two distinct pathways. The first involves multiphonon relaxation from the $^4\text{S}_{3/2}$ level, which itself is fed by ETU. The second occurs through the energy transfer process $(^4\text{I}_{11/2}, ^4\text{I}_{13/2}) \rightarrow (^4\text{F}_{9/2}, ^4\text{I}_{15/2})$.

These mechanisms are considered negligible and are not included in our model, as the $\text{Yb}^{3+} \rightarrow \text{Er}^{3+}$ ETU process is significantly more efficient in the dynamics of co-doped nanoparticles.

1 μm emission. The luminescence decays corresponding to the $^4\text{I}_{11/2} \rightarrow ^4\text{I}_{15/2}$ transition in Er^{3+} doped nanoparticles are presented in Figure 3.G.

The decay time measured on the 2% doped nanoparticles is slightly longer (1.8 ms) than the one obtained for 0.5% Er^{3+} nanoparticles (1.6 ms). This could be attributed to reabsorption effects, also known as radiation trapping,⁵² or to the up-conversion mechanism CR11 $(^4\text{I}_{13/2}, ^4\text{I}_{13/2}) \rightarrow (^4\text{I}_{9/2}, ^4\text{I}_{15/2})$,¹⁹ which may repopulate $^4\text{I}_{11/2}$ via multiphonon relaxation from the $^4\text{I}_{9/2}$ level, with the long-lived $^4\text{I}_{13/2}$ level serving as a reservoir. This non-resonant process, characterized by a energy mismatch of 628 cm^{-1} , could lengthen the lifetime of the $^4\text{I}_{11/2}$ level.

For higher doping levels, the decay times are significantly shortened, indicating important concentration quenching. This could be due to the up-conversion mechanism CR22 (${}^4\text{I}_{11/2}$, ${}^4\text{I}_{11/2}$) \rightarrow (${}^4\text{F}_{7/2}$, ${}^4\text{I}_{15/2}$) as introduced earlier. This mechanism depends quadratically on the population of the ${}^4\text{I}_{11/2}$ level, so a change in laser power should lead to a significant difference in the decay time. However, when the excitation power was experimentally reduced by a factor of 50, only small changes were observed, indicating that the significant concentration quenching is more likely due to migration and energy transfer to defects.

Figure 3.H shows the evolution of the relaxation rates K_2 as a function of Er^{3+} concentration. Although the number of data points is limited, the observed trend is similar to that of the Yb^{3+} transition. At lower concentrations, the quenching remains minimal, indicating a regime of limited diffusion. As the Er^{3+} concentration increases, a linear trend emerges, suggesting enhanced energy migration towards defects.

Once again, the modeling can be separated into two distinct regimes. For low Er^{3+} concentrations ($\leq 2\%$), no additional quenching processes are considered, and the relaxation rate is described by: $K_2 = k_{\text{R20}} + k_{\text{NR21}}$. A linear fit yields $k_{\text{NR21}} = 448 \text{ s}^{-1}$, where k_{R20} value was fixed. For higher Er^{3+} concentrations ($\geq 2\%$), an additional quenching term $k_{2\text{HC}}$ is introduced to account for increased energy transfer processes, leading to: $K_2 = k_{\text{R20}} + k_{\text{NR21}} + k_{2\text{HC}}n_0$. A fit, with only $k_{2\text{HC}}$ as a free parameter, gives $k_{2\text{HC}} = 9.4 \times 10^{-19} \text{ cm}^3.\text{s}^{-1}$.

The relaxation rates K_2 obtained from simulations are plotted in blue (low Er^{3+} regime) and pink (high Er^{3+} regime) in Figure 3.H. The model reliably reproduces the measured relaxation rates, particularly at low doping levels. Additionally, a slight decrease in the simulated relaxation rate is observed at low concentrations, primarily due to the inclusion of the CR11 mechanism in the simulation, since radiation trapping effects are not included in the modeling.

1.5 μm emission. Figure 3.I shows the luminescence decays corresponding to the transition ${}^4\text{I}_{13/2} \rightarrow {}^4\text{I}_{15/2}$ in Er-doped nanoparticles.

The luminescence decay measurements once again reveal a significant reduction in lifetime

with increasing Er^{3+} concentration. For a doping concentration of 0.5%, the measured lifetime is 8.1 ms, whereas it decreases to 0.09 ms for nanoparticles doped with 17%.

Moreover, while the 0.5 % Er-doped nanoparticles follows a mono-exponential trend, higher doping levels introduce a fast-decay component before stabilizing into a more mono-exponential behavior, as previously observed.

This quenching effect could be attributed to the up-conversion process CR11, discussed earlier. However, as with the $^4\text{I}_{11/2}$ level, no significant lifetime variation was observed upon reducing the excitation power, whereas a strong dependence would be expected if CR11 were the dominant quenching mechanism. This suggests that quenching primarily results from energy migration and transfer to defects.

Figure 3.J shows the evolution of the relaxation rates K_1 as a function of Er^{3+} concentration. Once again, the behavior follows a similar trend to the Yb^{3+} transition and the $^4\text{I}_{11/2} \rightarrow ^4\text{I}_{15/2}$ Er^{3+} transition. For the first regime of low Er^{3+} concentration ($\leq 2\%$), k_{10} —including both radiative and non-radiative rates—is adjusted by fitting K_1 following the relation $K_1 = k_{10}$, yielding $k_{10} = 186 \text{ s}^{-1}$. For the higher Er^{3+} concentration case, $k_{1\text{HC}}$ is introduced to take into account the quenching such as: $K_1 = k_{10} + k_{1\text{HC}}n_0$. A fit gives $k_{1\text{HC}} = 3.1 \times 10^{-18} \text{ cm}^3.\text{s}^{-1}$. The relaxation rates K_1 obtained from simulations, plotted in blue (low Er^{3+} concentration) and in pink (high Er^{3+} concentration) in Figure 3.J, accurately reproduces the experimental data, particularly at low doping levels. In this regime, a slight increase in the simulated relaxation rate with higher Er^{3+} concentrations is observed, which is attributed to the CR11 mechanism. The corresponding energy transfer rate was estimated by considering the energy gap ($\Delta E = 628 \text{ cm}^{-1}$), and its minimal impact on the relaxation rate further supports that quenching is primarily driven by other mechanisms, likely defect-related.

To summarize, the luminescence dynamics of Er-doped nanoparticles reveal strong concentration-dependent quenching, particularly affecting green and near-infrared emissions. At low Er^{3+} levels ($\leq 2\%$), the decay behavior aligns with high-quality reference materials and

is well-captured by linear models. At higher concentrations, additional quenching mechanisms—such as cross-relaxation and energy migration to defects—significantly shorten lifetimes. ETU among Er^{3+} ions contribute to long-tail decays. Overall, the simulated relaxation rates show good agreement with experimental data. The rate of the various relaxation paths extracted from experimental data are summarized in Table 3.

Table 3: Relaxation rates of Yb^{3+} and Er^{3+} excited states determined by fitting experimental data. *Radiative rates are taken from literature.²³

ion	level	*radiative rate (s^{-1})	non-radiative rate (s^{-1})	additional relaxation paths ($\text{cm}^3.\text{s}^{-1}$)	additional relaxation paths for concentration $>2\%$ ($\text{cm}^3.\text{s}^{-1}$)
Yb³⁺	$^2\text{F}_{5/2}$	$k_{1'0'}$ 173		$k_{\text{ET}1'0'\text{d}}$ 2.2×10^{-18}	/
Er³⁺	$^2\text{H}_{11/2}, ^4\text{S}_{3/2}$	$*k_{\text{R}50}$ 9.8×10^2 $*k_{\text{R}51}$ 4.2×10^2	$k_{\text{NR}54}$ 5.5×10^3	$k_{\text{CR}50}$ 4.9×10^{-17}	$k_{5\text{HC}}$ 1.6×10^{-16}
	$^4\text{F}_{9/2}$	$*k_{\text{R}40}$ 1.7×10^3	$k_{\text{NR}43}$ 5.5×10^4	/	/
	$^4\text{I}_{11/2}$	$*k_{\text{R}20}$ 1.5×10^2	$k_{\text{NR}21}$ 448	/	$k_{2\text{HC}}$ 9.4×10^{-19}
	$^4\text{I}_{13/2}$	k_{10} 186		/	$k_{1\text{HC}}$ 3.1×10^{-18}

Co-doped nanoparticles

After characterizing interactions within each ion species (Yb^{3+} – Yb^{3+} and Er^{3+} – Er^{3+}) and quantifying key processes such as NR decays and CR rates, we now turn to the investigation of co-doped nanoparticles. We investigate ET from Yb^{3+} to Er^{3+} as well as BT from Er^{3+} to Yb^{3+} . To this end, nanoparticles doped with 0.5% and 2% Er^{3+} , and varying Yb^{3+} concentrations, are analyzed to assess the influence of Yb^{3+} content on the excitation and relaxation dynamics. We begin by characterizing the key Er^{3+} energy levels through direct excitation (Figure 4), before examining their behavior under up-conversion excitation at 980 nm (Figure 5). Table 4 summarizes experimental lifetimes of various energy levels measured in the co-doped nanoparticles.

Table 4: Yb^{3+} and Er^{3+} excited state lifetimes (ms) for different doping concentrations in co-doped nanoparticles.

<i>ion</i>	<i>level</i>	<i>excitation</i>	Er concentration					
			0.5 %	0.5 %	2 %	2 %	2 %	2 %
			Yb concentration					
			2 %	5 %	5 %	7 %	9 %	17 %
Er^{3+}	$^2\text{H}_{11/2}, ^4\text{S}_{3/2}$	direct	0.058	0.035	0.030	0.019	0.016	0.011
		UC	0.41	0.21	0.19	0.09	0.05	0.01
	$^4\text{F}_{9/2}$	direct	0.018	0.017	0.017	0.016	0.016	0.013
		UC	0.26	0.18	0.19	0.11	0.08	0.03
Yb^{3+}	$^4\text{I}_{13/2}$	direct	7.8	7.4	6.7	4.4	6.6	4.3
	$^2\text{F}_{5/2}$	direct	0.66	0.34	0.53	0.23	0.20	0.07

Green emission - direct excitation. Figure 4.A (resp. 4.B) shows luminescence decays corresponding to the $^2\text{H}_{11/2}, ^4\text{S}_{3/2} \rightarrow ^4\text{I}_{15/2}$ transition in co-doped nanoparticles containing 0.5% Er^{3+} (resp. 2% Er) and varying Yb^{3+} concentrations.

An increase in Yb^{3+} concentration leads to a slight shortening of the decay times. For instance, in nanoparticles with 17% Yb, the lifetime τ is reduced by a factor of 4 compared to Yb-free nanoparticles. This quenching effect is attributed to the back transfer mechanism BT51 ($^4\text{S}_{3/2}, ^2\text{F}_{7/2} \rightarrow ^4\text{I}_{13/2}, ^2\text{F}_{5/2}$), with an energy gap of 1521 cm^{-1} . The large energy mismatch explains why concentration quenching remains relatively moderate.

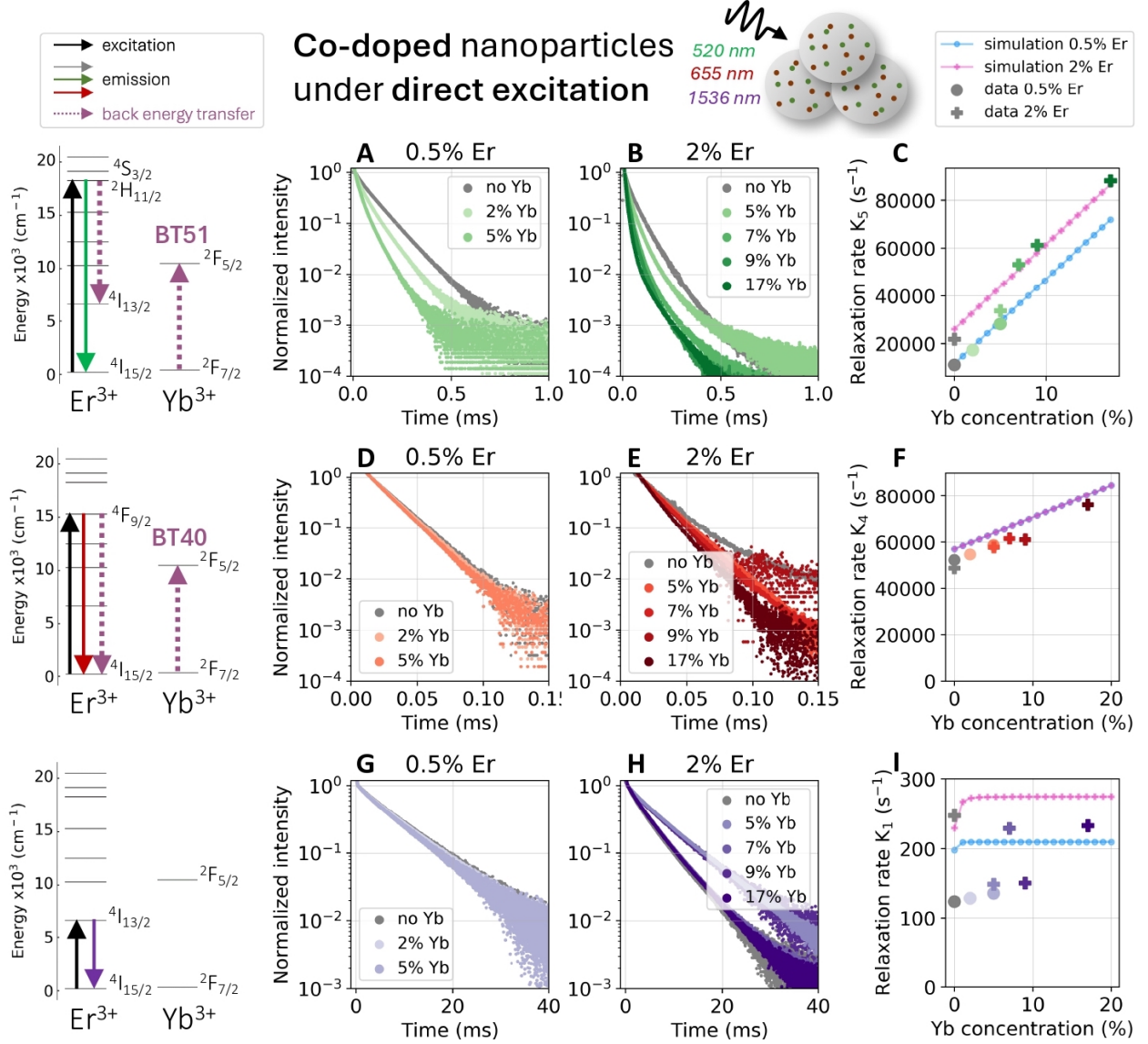


Figure 4: **Co-doped nanoparticles - under direct excitation.** (A,B) Luminescence decays of Er^{3+} green-emitting levels ($2H_{11/2}$, $4S_{3/2}$) of nanoparticles co-doped with 0.5 % and 2 % of Er. (C) Variation of the relaxation rate K_5 as a function of Yb^{3+} doping concentration. (D,E) Luminescence decays of Er^{3+} red-emitting level ($4F_{9/2}$) of nanoparticles co-doped with 0.5 % and 2 % of Er. (F) Variation of the relaxation rate K_4 as a function of Yb^{3+} concentration. (G,H) Luminescence decays of Er^{3+} 1.5 μm -emitting level ($4I_{13/2}$) of nanoparticles co-doped with 0.5 % and 2 % Er. (I) Variation of the relaxation rate K_1 as a function of Yb^{3+} concentration.

In the series of nanoparticles doped with 2% Er, a long tail appears in the luminescence decay, indicating an ETU process from the $2F_{5/2}$ level once it is populated by back transfer. This suggests that $2F_{5/2}$ acts as a reservoir with its long characteristic time.

Figure 3.C illustrates the variation of the relaxation rate K_5 as a function of Yb^{3+} concentration. For both Er^{3+} concentrations (0.5% and 2%), K_5 appears to vary linearly with Yb^{3+} concentration, which is consistent with the dominance of the BT mechanism. The relaxation rate can be expressed as: $K_5 = k_{\text{R}50} + k_{\text{R}51} + k_{\text{NR}54} + k_{\text{CR}50}n_0 + k_{\text{BT}51}n'_0$, where $k_{\text{BT}51}$ represents the energy transfer rate of BT51 mechanism. A linear fit, with $k_{\text{BT}51}$ as a free parameter, yields $k_{\text{BT}51} = 1.8 \times 10^{-17} \text{ cm}^3.\text{s}^{-1}$. The other parameters were fixed from the singly-doped nanoparticles section (see Table 2).

The relaxation rates K_5 obtained from the simulation, plotted in blue in Figure 3.C, show good agreement with experimental data for both series of Er^{3+} doping levels.

Red emission - direct excitation. Figure 4.D (resp. 4.E) shows luminescence decays corresponding to the $^4\text{F}_{9/2} \rightarrow ^4\text{I}_{15/2}$ transition in co-doped nanoparticles containing 0.5% Er^{3+} (resp. 2% Er) and varying Yb^{3+} concentrations.

Only a minor change is observed as the Yb^{3+} concentration increases. For example, in nanoparticles with 17% Yb , the lifetime τ is reduced by a factor of 1.5 compared to Yb -free nanoparticles. This quenching effect can be attributed to the back transfer mechanism BT40 ($^4\text{F}_{9/2}, ^2\text{F}_{7/2} \rightarrow ^4\text{I}_{15/2}, ^2\text{F}_{5/2}$), which has a large energy gap of 4979 cm^{-1} . The substantial energy mismatch explains why concentration quenching remains minimal.

Figure 3.F illustrates the variation of the relaxation rate K_4 as a function of Yb^{3+} concentration. For both Er^{3+} concentrations (0.5% and 2%), K_4 appears to vary linearly with Yb^{3+} concentration, indicating that the BT mechanism is the dominant process. We express: $K_4 = k_{\text{R}40} + k_{\text{NR}43} + k_{\text{BT}40}n'_0$, where $k_{\text{BT}40}$ is the energy transfer rate of BT40 process. A linear fit with $k_{\text{BT}40}$ as a free parameter, gives $k_{\text{BT}40} = 7.0 \times 10^{-18} \text{ cm}^3.\text{s}^{-1}$.

The simulation results in relaxation rates K_4 , plotted in blue in Figure 3.F, that are similar to the experimental data.

The visible emission spectra of the co-doped nanoparticles under 520 nm excitation (Figure S7) show an increasing R/G ratio with rising Yb^{3+} concentration, consistent with previous reports.^{20,55} As in the singly-doped samples, this trend is attributed to ion-ion interac-

tions that more efficiently populate the $^4F_{9/2}$ level at higher Yb^{3+} content, through pathways other than multiphonon relaxation from the $^2H_{11/2}$ and $^4S_{3/2}$ levels. In particular, the BT51 mechanism effectively populates both the $^4I_{13/2}$ and $^2F_{5/2}$ levels, enhancing the ETU process ($^4I_{13/2}, ^2F_{5/2} \rightarrow ^4F_{9/2}, ^2F_{7/2}$). Additionally, the CR51 interaction may also contribute to the observed increase in the R/G ratio. As a result of these mechanisms, the $^4F_{9/2}$ level becomes more populated relative to the $^4S_{3/2}$ level at high Yb^{3+} concentrations.

1.5 μm emission - direct excitation. Figure 4.G (resp. 4.H) shows luminescence decays corresponding to the $^4I_{13/2} \rightarrow ^4I_{15/2}$ transition in co-doped nanoparticles containing 0.5 % Er^{3+} (resp. 2% Er) and different Yb^{3+} concentrations.

Varying the Yb^{3+} concentration does not induce any significant change. The decay profiles of nanoparticles doped with 0.5% Er^{3+} remain nearly identical, with a lifetime of approximately 8 ms. In the case of nanoparticles doped with 2% Er, those containing 5% and 9% of Yb^{3+} exhibit slightly longer lifetimes (≈ 6.7 ms) compared to the others (≈ 4 ms). However, this variation is not systematically correlated with Yb^{3+} concentration, as shown in Figure 3.I, which depicts the relaxation rate K_1 as a function of Yb^{3+} content.

It is worth noting that energy level dynamics with such long lifetimes (on the order of several milliseconds) are highly sensitive to additional relaxation mechanisms, such as energy transfer to defects or impurities. Although the concentration of these defects and impurities may vary slightly between syntheses, potentially influencing the measured lifetimes, the nearly constant decay times observed as a function of Yb^{3+} concentration clearly rules out large increase of defect concentration in the co-doped particles.

The relaxation rates K_1 obtained from the simulation, plotted in blue in Figure 3.I, show relatively good agreement with experimental data for both series of Er^{3+} doping levels.

In summary, the luminescence decay times and relaxation rates of co-doped nanoparticles reveal distinct energy transfer mechanisms for different emission channels. While Yb^{3+} doping significantly affects green and red emissions through BT mechanisms, the long-lived 1.5 μm emission remains largely unaffected by Yb^{3+} concentration, evidencing a similar

concentration in quenching centers in all particles. This latter conclusion will be important in the following analyses. Table 5 summarizes the BT rates extracted from the experimental data.

Table 5: Back energy transfer rates ($\text{cm}^3.\text{s}^{-1}$) estimated from experimental data, and used for the modeling.

$$\begin{array}{c|c} k_{\text{BT51}} & k_{\text{BT40}} \\ \hline 1.8 \times 10^{-17} & 7.0 \times 10^{-18} \end{array}$$

1 μm emission - 980 nm excitation. Figure 5.A, 5.B, 5.C, and 5.D show luminescence decays corresponding to the $^2\text{F}_{5/2} \rightarrow ^2\text{F}_{7/2}$ transition in co-doped nanoparticles containing 2, 5, 9, 17 % Yb^{3+} and varying Er^{3+} concentrations.

The decays show that Yb^{3+} emission is slightly quenched by Er^{3+} which means that BT mechanisms are less efficient than Er^{3+} relaxations. In this case, Er^{3+} ions act as quenchers and reduces Yb^{3+} lifetime. This is also confirmed by the modeling showing a decreasing Yb^{3+} lifetime with increasing Er^{3+} concentration (Figure S10).

To quantitatively evaluate Yb-Er interactions, we will consider both decay of Yb^{3+} excited state and decays of the Er^{3+} green and red emitting levels, all after excitation of Yb^{3+} transition. This is needed because several ET and BT processes are involved in the dynamics of Yb^{3+} excited state.

Green emission - 980 nm excitation (ETU). Figure 5.F (resp. 5.G) shows luminescence decays corresponding to the $^2\text{H}_{11/2}, ^4\text{S}_{3/2} \rightarrow ^4\text{I}_{15/2}$ transition after up-conversion excitation in co-doped nanoparticles containing 0.5 % Er^{3+} (resp. 2 % Er) and varying Yb^{3+} concentrations. The ETU mechanism in Er^{3+} and Yb^{3+} co-doped materials is well known and occurs via two successive energy transfers from two excited Yb^{3+} ions to a nearby Er^{3+} ion.⁵⁶ The process is detailed in Supplementary Information.

As expected, it can be observed that the luminescence decay times of the different nanoparticles are longer in this case than when measured with direct excitation (see Figures 4.A and 4.B). For instance, nanoparticles doped with 2% Yb^{3+} and 0.5% Er^{3+} exhibit a

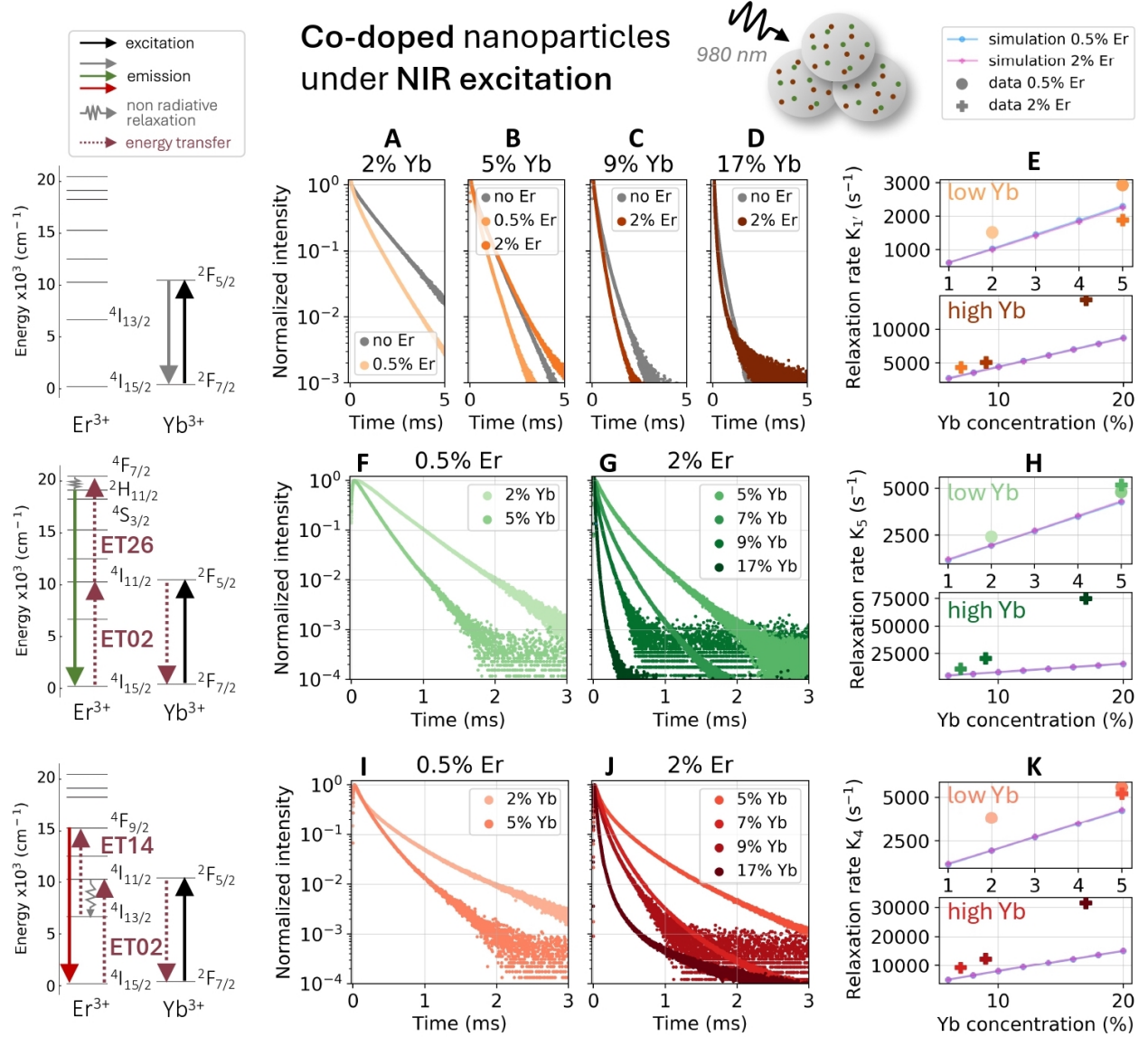


Figure 5: **Co-doped nanoparticles - under 980 nm excitation (ETU).** (A,B,C,D) Luminescence decays of Yb^{3+} excited state of nanoparticle singly-doped and co-doped with 2 %, 5 %, 9 % and 17% Yb. (E) Variation of the relaxation rate K_1' as a function of Yb^{3+} concentration. (F,G) Luminescence decays of Er^{3+} green-emitting levels ($2H_{11/2}$, $4S_{3/2}$) through ETU excitation of nanoparticles co-doped with 0.5 % and 2 % Er. (H) Variation of the relaxation rate K_5 as a function of Yb^{3+} concentration. (I,J) Luminescence decay of red-emitting level ($4F_{9/2}$) through ETU excitation of nanoparticles co-doped with 0.5 % and 2 % Er. (K) Variation of the relaxation rate K_4 as a function of Yb^{3+} concentration.

decay time of 0.41 ms with ETU excitation, compared to 0.058 ms under direct excitation.

This difference is attributed to the millisecond-range lifetimes of the Yb^{3+} excited state and the $4I_{11/2}$ level of Er, which serve as energy reservoirs in the process. This further confirms

that the levels are populated via ETU rather than excited-state absorption (ESA).

Additionally, the decay times of the $^2H_{11/2}$ and $^4S_{3/2}$ levels decrease with increasing Yb^{3+} concentration, as previously observed in ceramics,²⁵ and nanocrystals.²⁰ This trend is mainly attributed to the reduced lifetime of the $^2F_{5/2}$ level, which is already observed in singly-doped nanoparticles. However, additional mechanisms present in co-doped nanoparticles, such as ET and BT, also influence the overall dynamics. This is confirmed by the modeling indicating that increasing the Er^{3+} concentration leads to higher relaxation rates of the green-emitting levels through ETU excitation (Figure S11).

Optimizing UC luminescence requires balancing two competing effects: increasing rare-earth ion concentrations enhances absorption and energy transfer probability, but excessively high concentrations lead to concentration quenching, as observed in our study of singly-doped nanoparticles. Based on our results, a composition around 2% Yb^{3+} and 0.5% Er^{3+} likely provides an optimal trade-off for maximizing ETU efficiency. This hypothesis could be verified by quantitatively comparing the emission intensities across the different doping concentrations.

Red emission - 980 nm excitation (ETU). Figure 5.I (resp. 5.J) shows luminescence decays corresponding to the $^4F_{9/2} \rightarrow ^4I_{15/2}$ transition after NIR excitation in co-doped nanoparticles containing 0.5% Er^{3+} (resp. 2% Er) and varying Yb^{3+} concentrations.

As observed for the green-emitting levels, the $^4F_{9/2}$ level exhibits longer decay times through ETU excitation compared to direct excitation. For instance, nanoparticles doped with 2% Yb^{3+} and 0.5% Er^{3+} display a lifetime of approximately 0.26 ms when excited at 976 nm, whereas direct excitation at 655 nm results in a significantly shorter lifetime of 0.018 ms. These relatively long lifetimes further confirm that the red-emitting level is predominantly populated via energy transfer from longer-lived excited states.

Similar to the behavior of the $^2H_{11/2}$, $^4S_{3/2}$ levels, the fluorescence decay time of the $^4F_{9/2}$ level decreases with increasing Yb^{3+} concentration. This trend is primarily attributed to the reduction in the Yb^{3+} $^2F_{5/2}$ lifetime but also to other Yb^{3+} - Er^{3+} interactions since model-

ing shows that the red-emitting level lifetime decreases with increasing Er^{3+} concentration (Figure S12).

ETU modeling. To accurately model Yb–Er interactions following ETU excitation, we now focus on the key interactions: ET02, ET26, ET14, and BT20. Figure 5.E, 5.H and 5.K show the relaxation rates K_2 , K_5 , and K_4 as a function of Yb concentration, obtained from simulations using the following parameters: $k_{\text{ET02}} = k_{\text{ET26}} = 10^{-16} \text{ cm}^3 \cdot \text{s}^{-1}$, $k_{\text{ET14}} = 10^{-19} \text{ cm}^3 \cdot \text{s}^{-1}$, and $k_{\text{BT20}} = 10^{-15} \text{ cm}^3 \cdot \text{s}^{-1}$.

These ET and BT rates do not results from a fit, but were varied within a reasonable range (from 10^{-14} to $10^{-19} \text{ cm}^3 \cdot \text{s}^{-1}$), and no combination yielded significantly better agreement between the simulated and experimental data than those shown in Figure 5.E, 5.H, and 5.K. These parameters were found to be interdependent and also sensitive to the initial condition.

Comparing the simulation results with the experimental data, the model accurately reproduces the behavior observed at low to medium Yb^{3+} concentrations ($<5\%$) for both 0.5% and 2% Er. We thus obtain a comprehensive and accurate description of Er–Yb interactions in which energy transfer rates are mostly individually determined from specific measurements. In contrast with modeling where all parameters are simultaneously optimized, it can be expected that our approach leads to more reliable and physically meaningful parameters and in turn predictions of decay dynamics for a broad range of concentrations with fast computations. Interestingly, the fact that rate equations are able to reproduce experimental decay rates indicates that the microscopic variations in ions’ relative positions can be taken into account to a large extent by averaged values.

At very high Yb^{3+} concentrations, it can be noted that the experimental relaxation rates of all the three levels studied here, $^4\text{S}_{3/2}$, $^4\text{F}_{9/2}$, and $^2\text{F}_{5/2}$, are significantly faster than those predicted by the model (Figure 5, right column, lower graphs). As in the analysis of the singly-doped particles, this is attributed to the onset of fast energy migration between Yb^{3+} ions that effectively increases Er–Yb energy transfer rates. Thanks to our comprehensive study, a large increase of the concentration in quenching defects at high Yb^{3+} can be safely

dismissed given the nearly constant $^4I_{13/2}$ level decays observed in all co-doped particles.

Conclusion

In conclusion, we have investigated energy transfer in RE doped nanoparticles by studying the dynamics of multiple transitions, doping concentrations, and excitation paths, in order to achieve a broad understanding of the phenomena involved. Specifically, we studied Y_2O_3 nanoparticles of 100 nm diameter singly- or co-doped with Er^{3+} and Yb^{3+} in a broad range of concentrations extending from 0.5 to 17 at. %. First, PL decays were recorded for Er^{3+} green ($^4S_{3/2}, ^2H_{11/2} \rightarrow ^4I_{15/2}$), red ($^4F_{9/2} \rightarrow ^4I_{15/2}$) and IR ($^4I_{11/2} \rightarrow ^4I_{15/2}$, and $^4I_{13/2} \rightarrow ^4I_{15/2}$) transitions under direct excitation in the respective levels. The same experiment were performed on Yb^{3+} doped nanoparticles ($^2F_{5/2} \rightarrow ^2F_{7/2}$ transition). In a second series of experiments, transitions were studied in co-doped nanoparticles under direct excitation and then using ETU, a process of high interest for various applications.

In systems such as the one we studied, a large number of interactions between RE ions and defects can contribute to decay dynamics. To separate them and extract meaningful and usable values, we analyzed our decays using rate equations models and focused on reproducing the decay rates defined as $1/\tau$ where 2τ is the time for which the initial intensity has been reduced by $1/e^2 = 0.14$. This was chosen as a balance between short and long-time behaviors for non-exponential decays.

This modeling allowed us to reproduce direct excitation data and determine energy transfer relaxation rates in singly-doped nanoparticles in a broad range of concentrations. Energy transfers between RE ions but also towards quenching centers were taken into account, the latter being promoted by energy migration and thus important at high RE concentration. These relaxation rates were then used in the modeling of decays in co-doped particles, enabling extracting Er^{3+} - Yb^{3+} specific interactions and reproducing well experimental decays rates under direct excitation. For ETU, simulations are in good agreement with experiments up to Yb^{3+} concentrations of 5%. At levels above 10%, deviations were observed, as the

experimental decays were clearly shorter than predicted, and are attributed to fast energy migration between Yb^{3+} ions which increases Yb-Er energy transfer rates. Based on our analysis, a composition near 2% Yb^{3+} and 0.5% Er^{3+} appears optimal for maximizing ETU efficiency.

This work provides an exhaustive experimental study of interactions in a RE doped material and a modeling able to accurately predict decay rates of multiple transitions, in broad concentration ranges, and for different excitation paths. This approach opens the way to efficient optimization of PL in Er^{3+} , $\text{Yb}^{3+}:\text{Y}_2\text{O}_3$ nanoparticles and should be straightforward to extend to particles of different sizes, thin films, or transparent ceramics. More generally, it could be useful to analyze, design, and enhance RE doped materials in which emissions and excitations involve complex interactions.

Acknowledgement

This project has received funding from the European Research Council (ERC) under the European Union’s Horizon 2020 research and innovation programme (grant agreement No 101019234, RareDiamond) the 80 prime CNRS project Mathyq, and the USP-COFECUB programme (project Uc Ph-C 183/20).

Supporting Information Available

Synthesis of rare-earth doped Y_2O_3 nanoparticles

In a typical synthesis,⁴⁴ the required amounts of yttrium nitrate, erbium or ytterbium nitrate, and urea were dissolved in deionized water to a total volume of 252 mL, under vigorous magnetic stirring for 15 minutes at room temperature, within a Teflon reactor. The sealed reactor was then subjected to hydrothermal treatment in a drying oven at 85 °C for 24 hours.

Following the reaction, the resulting precipitate was collected by centrifugation at 13,000 rpm for 10 minutes at 4 °C, using multiple washing steps with deionized water to remove the byproducts. Anhydrous ethanol was used for the final washing of the nanoparticles. The precursor was suspended in anhydrous ethanol and subsequently dried at 80 °C for 24 hours to obtain $\text{Y}(\text{OH})\text{CO}_3 \cdot n\text{H}_2\text{O}$. Crystalline $\text{Y}_2\text{O}_3\text{:RE}^{3+}$ nanoparticles ($\text{RE}^{3+} = \text{Er}^{3+}$ or Yb^{3+}) were formed via two-step annealing, initially at 800 °C for 6 hours, followed by a second treatment at 1200 °C for 18 hours using a heating rate of 3 °C. min⁻¹.

Simulation

Radiative and non-radiative relaxation rates

Radiative rates from each excited state level and branching ratio are taken from literature.^{23,41} Non-radiative decay rates are estimated from low-concentration experiments or fitted experimental data. The parameters are displayed in Table 6.

Table 6: Radiative and non-radiative relaxation rates (s⁻¹) of Er^{3+} and Yb^{3+} ions used for the modeling.

$k_{\text{R}51}$ 4.2×10^2	$k_{\text{R}50}$ 9.8×10^2	$k_{\text{R}40}$ 1.7×10^3	$k_{\text{R}30}$ 2.2×10^2	$k_{\text{R}20}$ 1.5×10^2	k_{10} 186
$k_{\text{NR}65}$ 1×10^7	$k_{\text{NR}54}$ 5.5×10^3	$k_{\text{NR}43}$ 5.5×10^4	$k_{\text{NR}32}$ 3.8×10^5	$k_{\text{NR}21}$ 448	$k_{1'0'}$ 173

Energy transfer rates

Some of the energy transfer rates such as $k_{\text{ET1}'0'd}$, k_{CR50} , $k_{5\text{HC}}$, $k_{2\text{HC}}$, $k_{1\text{HC}}$, k_{BT51} and k_{BT40} have been determined directly from experimental data and are reminded in Table 7.

Table 7: Energy transfer rates ($\text{cm}^3 \cdot \text{s}^{-1}$) estimated from experimental data used for the modeling.

$$\begin{array}{c|c|c|c|c|c|c} k_{\text{ET1}'0'd} & k_{\text{CR50}} & k_{\text{BT51}} & k_{\text{BT40}} & k_{5\text{HC}} & k_{2\text{HC}} & k_{1\text{HC}} \\ \hline 2.2 \times 10^{-18} & 4.9 \times 10^{-17} & 1.8 \times 10^{-17} & 7.0 \times 10^{-18} & 1.6 \times 10^{-16} & 9.4 \times 10^{-19} & 3.1 \times 10^{-18} \end{array}$$

Key energy transfer rates for UC mechanism such as k_{ET02} , k_{ET26} , k_{ET14} , k_{BT20} have been fixed by comparing experimental data with simulation results and are reported in Table 8.

Table 8: Energy transfer rates ($\text{cm}^3 \cdot \text{s}^{-1}$) estimated from experimental data used for the modeling.

$$\begin{array}{c|c|c|c} k_{\text{ET02}} & k_{\text{ET26}} & k_{\text{ET14}} & k_{\text{BT20}} \\ \hline 10^{-16} & 10^{-16} & 10^{-19} & 10^{-15} \end{array}$$

A wide variety of other ion-ion interactions can occur, due to the large number of available energy levels in Er^{3+} ions. To simplify simulations and improve the interpretability of the mechanisms involved, it is useful to limit the model to the dominant interactions. This selection can be guided by the energy gaps associated with the transfers, as well as by previously conducted experimental analyses.

The probability of an energy transfer involving a mismatch ΔE decreases exponentially as $\exp(-\beta\Delta E)$, where β is a material-dependent parameter. For Y_2O_3 matrices, β has been estimated to be $2.5 \times 10^{-3} \text{ cm}$.⁴² In that study, conducted at 77 K, the probability of resonant energy transfer was evaluated to be approximately 10^5 s^{-1} for a donor concentration of 4%, corresponding to about $7 \times 10^{20} \text{ cm}^{-3}$. This implies a resonant energy transfer coefficient of $k_{\text{ET}} \approx 1.4 \times 10^{-16} \text{ cm}^3 \cdot \text{s}^{-1}$.

Although this approximation does not explicitly account for the variation in coupling strengths between different transitions, it offers a reasonable estimate in most cases.⁴²

The remaining energy transfer rates, which could not be determined experimentally, are

estimated using this method and are reported in Table 9.

Table 9: Energy transfer rates estimated based on the energy gap.

	transition 1	transition 2	$\frac{\Delta E}{(\text{cm}^{-1})}$	notation	rate ($\text{cm}^3.\text{s}^{-1}$)
back energy transfer	${}^4\text{F}_{7/2} \rightarrow {}^4\text{I}_{11/2}$	${}^2\text{F}_{7/2} \rightarrow {}^2\text{F}_{5/2}$	100	k_{BT62}	1.4×10^{-16}
$\text{Er}^{3+} \rightarrow \text{Yb}^{3+}$	${}^4\text{F}_{9/2} \rightarrow {}^4\text{I}_{13/2}$	${}^2\text{F}_{7/2} \rightarrow {}^2\text{F}_{5/2}$	-1479		0
	${}^4\text{F}_{7/2} \rightarrow {}^4\text{I}_{11/2}$	${}^4\text{I}_{15/2} \rightarrow {}^4\text{I}_{11/2}$	119		0
	${}^4\text{I}_{11/2} \rightarrow {}^4\text{I}_{15/2}$	${}^4\text{I}_{11/2} \rightarrow {}^4\text{F}_{7/2}$	-119		0
cross-relaxation	${}^4\text{F}_{7/2} \rightarrow {}^4\text{F}_{9/2}$	${}^4\text{I}_{11/2} \rightarrow {}^4\text{F}_{9/2}$	196	k_{CR62}	1.4×10^{-16}
$\text{Er}^{3+} \rightarrow \text{Er}^{3+}$	${}^2\text{H}_{11/2} \rightarrow {}^4\text{F}_{9/2}$	${}^4\text{I}_{13/2} \rightarrow {}^4\text{I}_{11/2}$	245	k_{CR51}	1.4×10^{-16}
	${}^4\text{I}_{11/2} \rightarrow {}^4\text{I}_{13/2}$	${}^4\text{F}_{9/2} \rightarrow {}^4\text{S}_{3/2}$	615	k_{CR42}	3.0×10^{-17}
	${}^4\text{I}_{13/2} \rightarrow {}^4\text{I}_{15/2}$	${}^4\text{I}_{13/2} \rightarrow {}^4\text{I}_{9/2}$	628	k_{CR11}	2.9×10^{-17}

The cross-relaxation process (${}^4\text{I}_{11/2}, {}^4\text{I}_{11/2}$) \rightarrow (${}^4\text{I}_{15/2}, {}^4\text{F}_{7/2}$), as well as its reverse process (${}^4\text{F}_{7/2}, {}^4\text{I}_{15/2}$) \rightarrow (${}^4\text{I}_{11/2}, {}^4\text{I}_{11/2}$), can be considered negligible. These mechanisms are analogous to the direct energy transfer (${}^2\text{F}_{5/2}, {}^4\text{I}_{11/2}$) \rightarrow (${}^2\text{F}_{7/2}, {}^4\text{F}_{7/2}$) and the back energy transfer (${}^4\text{F}_{7/2}, {}^2\text{F}_{7/2}$) \rightarrow (${}^4\text{I}_{11/2}, {}^2\text{F}_{5/2}$) involving Yb^{3+} ions, but are less likely to occur since the ${}^4\text{I}_{15/2} \rightarrow {}^4\text{I}_{11/2}$ transition is approximately seven times weaker than the ${}^2\text{F}_{7/2} \rightarrow {}^2\text{F}_{5/2}$ transition.²³

Rate equations

The population rate equations used in the modeling are the following:⁴⁰

$$\frac{dn_{1'}}{dt} = -k_{1'0'}n_{1'} - k_{ET02}n_0n_{1'} - k_{ET26}n_2n_{1'} - k_{ET14}n_1n_{1'} \quad (2)$$

$$+ k_{BT20}n_2n_{0'} + k_{BT62}n_6n_{0'} + k_{BT51}n_5n_{0'} + k_{BT40}n_4n_{0'} \\ - k_{ET1'0'd}n_{0'}n_{1'}$$

$$\frac{dn_{0'}}{dt} = +k_{1'0'}n_{1'} + k_{ET02}n_0n_{1'} + k_{ET26}n_2n_{1'} + k_{ET14}n_1n_{1'} \quad (3)$$

$$- k_{BT20}n_2n_{0'} - k_{BT62}n_6n_{0'} - k_{BT51}n_5n_{0'} - k_{BT40}n_4n_{0'} \\ + k_{ET1'0'd}n_{0'}n_{1'}$$

$$\frac{dn_6}{dt} = -k_{NR65}n_6 + k_{ET26}n_2n_{1'} - k_{BT62}n_{0'}n_6 - k_{CR62}n_2n_6 \quad (4)$$

$$\frac{dn_5}{dt} = +k_{NR65}n_6 - k_{R51}n_5 - k_{R50}n_5 - k_{NR54}n_5 \quad (5)$$

$$- k_{BT51}n_{0'}n_5 - k_{CR51}n_1n_5 - k_{CR50}n_0n_5 + k_{CR42}n_4n_2 \\ (-k_{5HC}n_0n_5)$$

$$\frac{dn_4}{dt} = +k_{NR54}n_5 - k_{R40}n_4 - k_{NR43}n_4 + k_{ET14}n_1n_{1'} \quad (6)$$

$$+ 2k_{CR62}n_6n_2 + k_{CR51}n_1n_5 - k_{CR42}n_2n_4 - k_{BT40}n_{0'}n_4$$

$$\frac{dn_3}{dt} = +k_{NR43}n_4 - k_{R30}n_3 - k_{NR32}n_3 + k_{CR50}n_5n_0 + k_{CR11}n_1n_1 \quad (7)$$

$$\frac{dn_2}{dt} = +k_{NR32}n_3 - k_{R20}n_2 - k_{NR21}n_2 + k_{ET02}n_0n_{1'} \quad (8)$$

$$- k_{ET26}n_{1'}n_2 + k_{BT62}n_{0'}n_6 - k_{BT20}n_{0'}n_2 - k_{CR62}n_6n_2 \\ - k_{CR42}n_4n_2 + k_{CR51}n_5n_1(-k_{2HC}n_0n_2)$$

$$\frac{dn_1}{dt} = +k_{NR21}n_2 + k_{R51}n_5 - k_{10}n_1 - k_{ET14}n_{1'}n_1 \quad (9)$$

$$+ k_{BT51}n_{0'}n_5 - k_{CR51}n_5n_1 + k_{CR50}n_5n_0 \\ + k_{CR42}n_4n_2 - 2k_{CR11}n_1n_1(-k_{1HC}n_0n_1)$$

$$\frac{dn_0}{dt} = +k_{R50}n_5 + k_{R40}n_4 + k_{R30}n_3 + k_{R20}n_2 + k_{10}n_1 \quad (10)$$

$$- k_{ET02}n_{1'}n_0 + k_{BT20}n_{0'}n_2 + k_{BT40}n_{0'}n_4 - k_{CR50}n_5n_0 \\ + k_{CR11}n_1n_1(+k_{5HC}n_0n_5 + k_{2HC}n_0n_2 + k_{1HC}n_0n_1)$$

with the following conditions : $\sum_{i=0}^{n-1} n_i = N_{Er}$ et $n_{0'} + n_{1'} = N_{Yb}$ and the initial conditions. We consider at $t = 0$ that the excited state is populated with 1% of the ions.

The energy transfer rates k_{5HC} , k_{2HC} , and k_{1HC} are used exclusively in the simulation of nanoparticles with Er^{3+} doping concentrations $> 5\%$.

Yb excited state decays fitted with Inokuti model

Inokuti and Hirayama modeled the energy transfer dynamics in the case of dipole–dipole interactions between donors (ions excited at $t = 0$) and acceptors (ions or defects not excited at $t = 0$ that receive the transferred energy) using the following expression:¹⁵

$$I(t) = I_0 \exp\left(-\frac{4}{3}\pi^{3/2}N_A\sqrt{Ct}\right)\exp(-t/\tau) \quad (11)$$

where N_A is the acceptor concentration, C represents the strength of the donor–acceptor interaction, and τ accounts for both the intrinsic donor lifetime τ_0 and the energy migration lifetime τ_D due to donor–donor energy transfer before reaching an acceptor: $1/\tau = 1/\tau_0 + 1/\tau_D$. The first exponential term, which varies with \sqrt{t} , leads to a rapid drop in luminescence at short times, while the second term results in a mono-exponential decay at longer times.

To account for the distribution of donor environments in Yb^{3+} -doped systems, luminescence decays were fitted using Equation 11. The decay time τ was first estimated by fitting the tail of the decay curve with a mono-exponential function. Then, the parameter $N_A\sqrt{C}$ was fitted to capture the deviation from exponential behavior at short times.

Table 10 summarizes the fitting parameters used in the analysis.

Table 10: Parameters used to fit the luminescence decays in Figure 6.

	0.5% Yb	1% Yb	2% Yb	5% Yb	9% Yb	17% Yb
τ (ms)	1.24	1.32	1.25	0.655	0.538	0.347
$N_A\sqrt{C}$ (s ^{-1/2})	9.6×10^{-4}	7.9×10^{-4}	6.2×10^{-4}	1.6×10^{-3}	6.0×10^{-3}	1.1×10^{-2}

As shown in Figure 6, the Inokuti–Hirayama model provides a reasonably good fit to the experimental decay curves across the range of doping levels. More advanced models, such

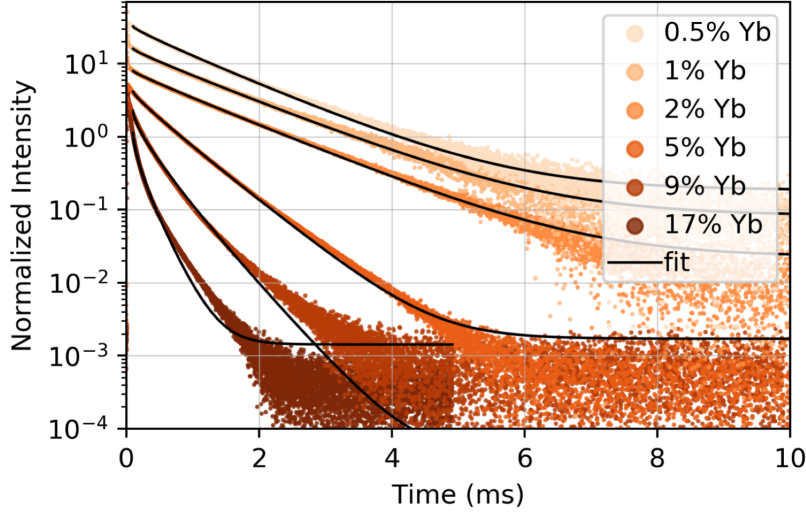


Figure 6: Luminescence decays of the Yb^{3+} excited state level for various doping levels, fitted using the model developed by Inokuti and Hirayama. The decays are vertically shifted for clarity.

as the one proposed by Yokota and Tanimoto,¹⁴ were not used, as they introduce additional free parameters without significantly improving the quality of the fit.

Visible emission spectra of co-doped nanoparticles under 520 nm excitation

Figure 7 shows the visible emission spectra of co-doped nanoparticles under 520 nm excitation. The emission bands are similar to those observed in Er^{3+} -only doped nanoparticles, with peaks around 550 nm—corresponding to the $^2\text{H}_{11/2}$, $^4\text{S}_{3/2} \rightarrow ^4\text{I}_{15/2}$ transitions—and around 660 nm, associated with the $^4\text{F}_{9/2} \rightarrow ^4\text{I}_{15/2}$ transition (see Figure 2.E). A clear increase in the R/G ratio is observed with increasing Yb^{3+} concentration, indicating a strong influence of Yb^{3+} on the population dynamics of the $^2\text{H}_{11/2}$, $^4\text{S}_{3/2}$, and $^4\text{F}_{9/2}$ levels. This effect is likely driven by specific interactions such as BT51 and CR51 (see Figure 4).

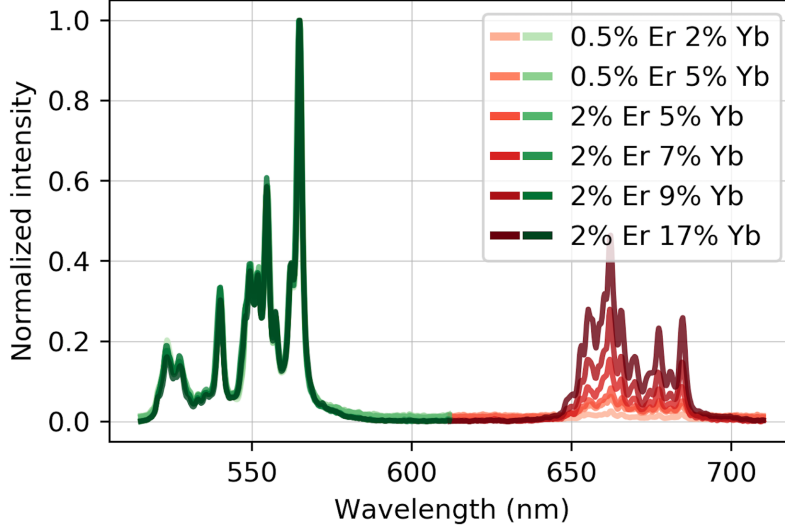


Figure 7: Emission spectra of the co-doped nanoparticles in the visible range following excitation at 520 nm.

Visible emission spectra of co-doped nanoparticles under 980 nm excitation

Figure 8 shows the visible emission spectra of co-doped nanoparticles under 980 nm excitation. Emission bands are observed around 550 nm, corresponding to the ${}^2\text{H}_{11/2}$, ${}^4\text{S}_{3/2} \rightarrow {}^4\text{I}_{15/2}$ transitions, and around 660 nm, corresponding to the ${}^4\text{F}_{9/2} \rightarrow {}^4\text{I}_{15/2}$ transition. These features confirm the occurrence of UC process between Yb^{3+} and Er^{3+} ions.

Under near-infrared excitation, green-emitting levels of Er^{3+} ions are populated via ETU from Yb^{3+} ions.⁵⁶ This process involves two sequential energy transfers: first, $({}^2\text{F}_{5/2}^{\text{Yb}}, {}^4\text{I}_{15/2}^{\text{Er}}) \rightarrow ({}^2\text{F}_{7/2}^{\text{Yb}}, {}^4\text{I}_{11/2}^{\text{Er}})$, then $({}^2\text{F}_{5/2}^{\text{Yb}}, {}^4\text{I}_{11/2}^{\text{Er}}) \rightarrow ({}^2\text{F}_{7/2}^{\text{Yb}}, {}^4\text{F}_{7/2}^{\text{Er}})$, followed by non-radiative relaxation to the green-emitting levels (${}^2\text{H}_{11/2}$, ${}^4\text{S}_{3/2}$). In parallel, the ${}^4\text{I}_{13/2}$ level can be populated via non-radiative decay from ${}^4\text{I}_{11/2}$. Then, another ET $({}^2\text{F}_{5/2}^{\text{Yb}}, {}^4\text{I}_{13/2}^{\text{Er}}) \rightarrow ({}^2\text{F}_{7/2}^{\text{Yb}}, {}^4\text{F}_{9/2}^{\text{Er}})$ populates the red-emitting level ${}^4\text{F}_{9/2}$. In Y_2O_3 materials, this pathway is the dominant mechanism for red emission. In contrast, for other host crystals, the red-emitting level is populated by non-radiative relaxation from the green-emitting levels, themselves populated via ETU as previously described.⁵⁷

Compared to direct excitation of the ${}^2\text{H}_{11/2}$ and ${}^4\text{S}_{3/2}$ levels—where the green emission

dominates over red emission (see Figure 7)—the reversed intensity ratio observed here confirms that the $^4F_{9/2}$ level is not mainly populated by energy transfer from the $^4I_{13/2}$ level.

An increase of the R/G ratio with increasing Yb^{3+} concentration can be attributed to the BT51 mechanism that depopulates efficiently the green-emitting levels at high Yb^{3+} concentration.

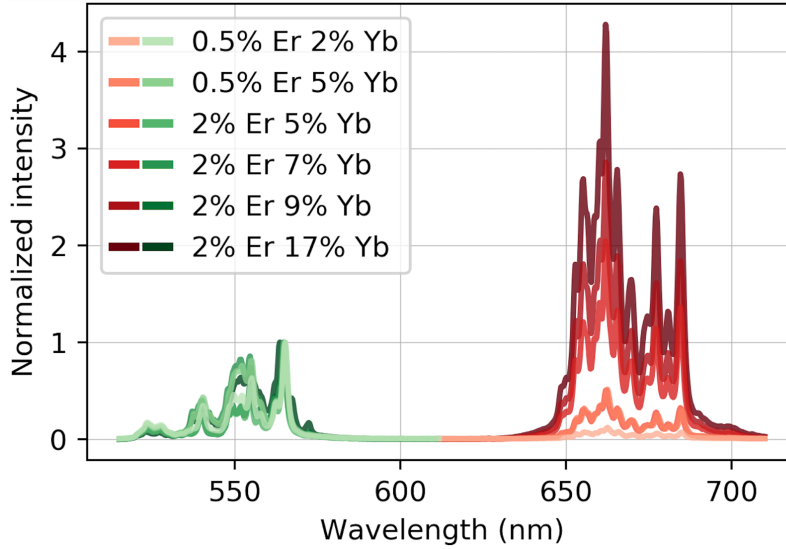


Figure 8: Emission spectra of the co-doped nanoparticles in the visible range following excitation at 980 nm.

Modeling of green luminescence decay following up-conversion excitation

Figure 9 presents the fluorescence decays of the green-emitting levels through ETU excitation in co-doped nanoparticles. The simulated decay curves (dashed blue lines) show good agreement with the experimental data.

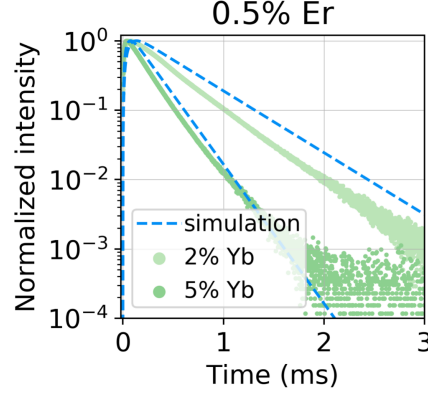


Figure 9: Green-emitting levels decays of co-doped nanoparticles following excitation at 980 nm and the associated modeling.

Variation of excited state lifetimes under NIR excitation as a function of Er concentration

Figure 10 presents the relaxation rate K_1 , as a function of Er concentration, for nanoparticles co-doped with 2% Yb and 5% Yb. The modeling shows that increasing Er concentration leads to shortening of Yb^{3+} lifetime, confirming that Er^{3+} ions act as quenching centers for Yb^{3+} ions.

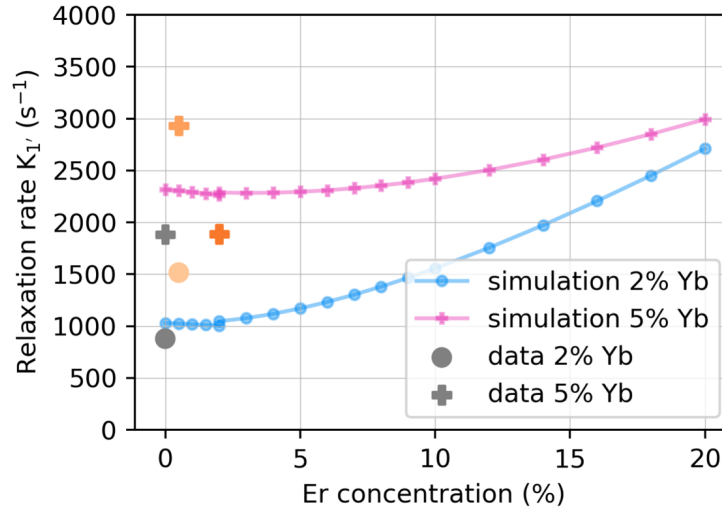


Figure 10: Relaxation rate of the Yb^{3+} excited state level following excitation at 980 nm for co-doped nanoparticles with 2% Yb and 5% Yb as a function of Er concentration.

Figure 11 and Figure 12 present the relaxation rate K_5 of the green-emitting levels

($^2H_{11/2}, ^4S_{3/2}$) and the relaxation rate K_4 of the red-emitting level ($^4F_{9/2}$), as a function of Er concentration, for nanoparticles co-doped with 2% Yb and 5% Yb. The modeling shows that relaxation rates of both levels increases with Er increasing.

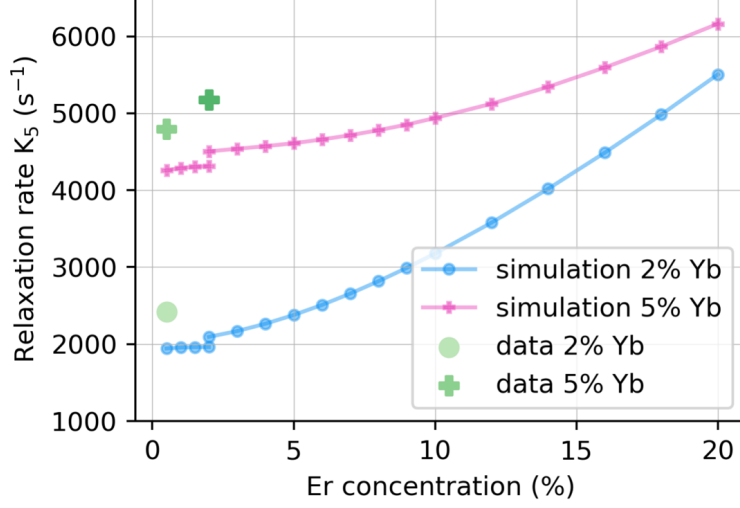


Figure 11: Relaxation rate of the $^2H_{11/2}, ^4S_{3/2}$ levels following excitation at 980 nm for co-doped nanoparticles with 2% Yb and 5% Yb as a function of Er concentration.

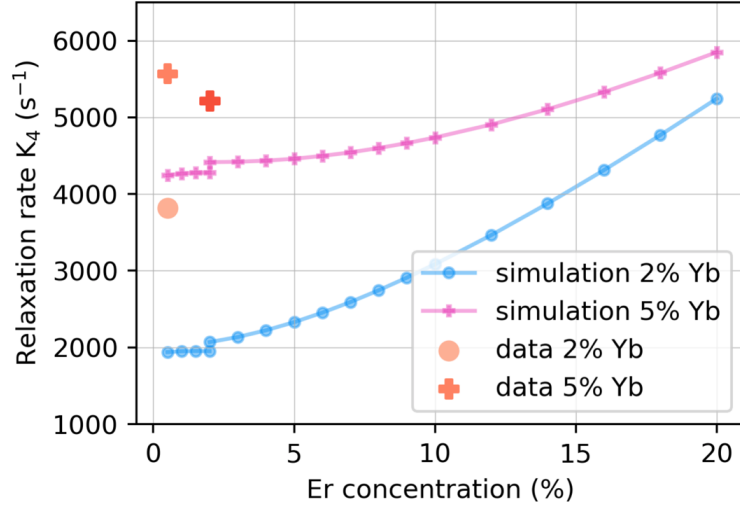


Figure 12: Relaxation rate of the $^4F_{9/2}$ level following excitation at 980 nm for co-doped nanoparticles with 2% Yb and 5% Yb as a function of Er concentration.

References

- (1) Weber, M. J. *Luminescence Decay by Energy Migration and Transfer: Observation of Diffusion-Limited Relaxation*; 1971; Vol. 4.
- (2) Huber, D. L. *Laser Spectroscopy of Solids*; Springer, Berlin, Heidelberg, 1981; pp 83–111.
- (3) Mangnus, M. J. J.; Zom, J.; Welling, T. A. J.; Meijerink, A.; Rabouw, F. T. Finite-Size Effects on Energy Transfer between Dopants in Nanocrystals. *ACS Nanoscience Au* **2022**, *2*, 111–118.
- (4) Auzel, F. Compteur quantique par transfert d’énergie entre deux ions de terres rares dans un tungstate mixte et dans un verre. *CR Acad. Sci. Paris* **1966**, *262*, 1016–1019.
- (5) Wright, J. C. *Radiationless Processes in Molecules and Condensed Phases*; Springer Berlin Heidelberg: Berlin, Heidelberg, 1976; Vol. 15; pp 239–295.
- (6) Gai, S.; Li, C.; Yang, P.; Lin, J. Recent Progress in Rare Earth Micro/Nanocrystals: Soft Chemical Synthesis, Luminescent Properties, and Biomedical Applications. *Chemical Reviews* **2014**, *114*, 2343–2389.
- (7) Du, K.; Feng, J.; Gao, X.; Zhang, H. Nanocomposites Based on Lanthanide-Doped Upconversion Nanoparticles: Diverse Designs and Applications. *Light: Science & Applications* **2022**, *11*, 222.
- (8) Lee, C.; Xu, E. Z.; Liu, Y.; Teitelboim, A.; Yao, K.; Fernandez-Bravo, A.; Kotulska, A. M.; Nam, S. H.; Suh, Y. D.; Bednarkiewicz, A.; Cohen, B. E.; Chan, E. M.; Schuck, P. J. Giant Nonlinear Optical Responses from Photon-Avalanching Nanoparticles. *Nature* **2021**, *589*, 230–235.
- (9) Scheife, H.; Huber, G.; Heumann, E.; Bär, S.; Osiac, E. Advances in Up-Conversion Lasers Based on Er³⁺ and Pr³⁺. *Optical Materials* **2004**, *26*, 365–374.

- (10) Caixeta, F. J.; Bastos, A. R. N.; Botas, A. M. P.; Rosa, L. S.; Souza, V. S.; Borges, F. H.; Neto, A. N. C.; Ferrier, A.; Goldner, P.; Carlos, L. D.; Gonçalves, R. R.; Ferreira, R. A. S. High-Quantum-Yield Upconverting $\text{Er}^{3+}/\text{Yb}^{3+}$ -Organic-Inorganic Hybrid Dual Coatings for Real-Time Temperature Sensing and Photothermal Conversion. *The Journal of Physical Chemistry C* **2020**, *124*, 19892–19903.
- (11) Zeng, X. et al. Visualization of Intra-neuronal Motor Protein Transport through Upconversion Microscopy. *Angewandte Chemie International Edition* **2019**, *58*, 9262–9268.
- (12) Bednarkiewicz, A.; Chan, E. M.; Kotulska, A.; Marciniak, L.; Prorok, K. Photon Avalanche in Lanthanide Doped Nanoparticles for Biomedical Applications: Super-Resolution Imaging. *Nanoscale Horizons* **2019**, *4*, 881–889.
- (13) Kushida, T. Energy Transfer and Cooperative Optical Transitions in Rare-Earth Doped Inorganic Materials. I. Transition Probability Calculation. *Journal of the Physics Society Japan* **1973**, *34*, 1318–1326.
- (14) Yokota, M.; Tanimoto, O. Effects of diffusion on energy transfer by resonance. *Journal of the physical society of Japan* **1967**, *22*, 779–784.
- (15) Inokuti, M.; Hirayama, F. Influence of energy transfer by the exchange mechanism on donor luminescence. *The Journal of Chemical Physics* **1965**, *43*, 1978–1989.
- (16) Villanueva-Delgado, P.; Krämer, K. W.; Valiente, R. Simulating Energy Transfer and Upconversion in $\beta\text{-NaYF}_4\text{: Yb}^{3+}, \text{Tm}^{3+}$. *The Journal of Physical Chemistry C* **2015**, *119*, 23648–23657.
- (17) Goldner, P.; Pellé, F. Photon Avalanche Fluorescence and Lasers. *Optical Materials* **1996**, *5*, 239–249.
- (18) Wen, S.; Zhou, J.; Zheng, K.; Bednarkiewicz, A.; Liu, X.; Jin, D. Advances in highly doped upconversion nanoparticles. *Nature communications* **2018**, *9*, 2415.

- (19) Hossan, M. Y.; Hor, A.; Luu, Q.; Smith, S. J.; May, P. S.; Berry, M. T. Explaining the Nanoscale Effect in the Upconversion Dynamics of β -NaYF₄:Yb³⁺, Er³⁺ Core and Core-Shell Nanocrystals. *Journal of Physical Chemistry C* **2017**, *121*, 16592–16606.
- (20) Vetrone, F.; Boyer, J. C.; Capobianco, J. A.; Speghini, A.; Bettinelli, M. Significance of Yb³⁺ concentration on the upconversion mechanisms in codoped Y₂O₃:Er³⁺, Yb³⁺ nanocrystals. *Journal of Applied Physics* **2004**, *96*, 661–667.
- (21) Mialon, G.; Türkcan, S.; Alexandrou, A.; Gacoin, T.; Boilot, J. P. New Insights into Size Effects in Luminescent Oxide Nanocrystals. *The Journal of Physical Chemistry C* **2009**, *113*, 18699–18706.
- (22) Chen, X.; Peng, D.; Ju, Q.; Wang, F. Photon Upconversion in Core–Shell Nanoparticles. *Chemical Society Reviews* **2015**, *44*, 1318–1330.
- (23) Weber, M. J. Radiative and Multiphonon Relaxation of Rare-Earth Ions in Y₂O₃. 1968.
- (24) Mun, J.; Jouini, A.; Guyot, Y.; Yoshikawa, A.; Ohta, H.; Shibata, H.; Waseda, Y.; Boulon, G.; Fukuda, T. Growth and Characterization of Tm-doped Y₂O₃ Single Crystals. *Optical Materials* **2007**, *29*, 1390–1393.
- (25) Kimura, H.; Kato, T.; Yamamoto, S.-i.; Nakauchi, D.; Kawaguchi, N.; Yanagida, T. Influence of Yb doping on optical and upconversion photoluminescence properties of Yb-, Er-co-doped Y₂O₃ transparent ceramics prepared by SPS. *Journal of Materials Science: Materials in Electronics* **2021**, *32*, 6304–6311.
- (26) Brown, E. E.; Hömmerich, U.; Bluiett, A.; Kucera, C.; Ballato, J.; Trivedi, S. Near-infrared and upconversion luminescence in Er:Y₂O₃ ceramics under 1.5 μ m excitation. *Journal of the American Ceramic Society* **2014**, *97*, 2105–2110.
- (27) Harada, N.; Ferrier, A.; Serrano, D.; Persechino, M.; Briand, E.; Bachelet, R.; Vickridge, I.; Ganem, J.-J.; Goldner, P.; Tallaire, A. Chemically vapor deposited

- Eu³⁺:Y₂O₃ thin films as a material platform for quantum technologies. *Journal of Applied Physics* **2020**, *128*, 055304.
- (28) Liu, S.; Fossati, A.; Serrano, D.; Tallaire, A.; Ferrier, A.; Goldner, P. Defect Engineering for Quantum Grade Rare-Earth Nanocrystals. *ACS Nano* **2020**, *14*, 9953–9962.
- (29) Vetrone, F.; Boyer, J.-C.; Capobianco, J. A.; Speghini, A.; Bettinelli, M. Concentration-dependent near-infrared to visible upconversion in nanocrystalline and bulk Y₂O₃:Er³⁺. *Chemistry of materials* **2003**, *15*, 2737–2743.
- (30) Tian, Y.; Fu, Y.; Xing, M.; Luo, X. Upconversion Luminescence Properties of Y₂O₃:Yb, Er and Y₂O₂S:Yb, Er Nanoparticles Prepared by Complex Precipitation. *Journal of Nanomaterials* **2015**, *2015*.
- (31) Sanamyan, T.; Kanskar, M.; Xiao, Y.; Kedlaya, D.; Dubinskii, M. High Power Diode-Pumped 2.7-Mm Er³⁺:Y₂O₃ Laser with Nearly Quantum Defect-Limited Efficiency. *Optics Express* **2011**, *19*, A1082–A1087.
- (32) Molina, P.; Sommer, M.; Kattner, F.; Henniger, J. Response Characterization of an Y₂O₃:Eu-based Radioluminescence Probe under ⁶⁰Co Irradiation. *Radiation Measurements* **2013**, *56*, 338–341.
- (33) Chávez-García, D.; Sengar, P.; Juárez-Moreno, K.; Flores, D. L.; Calderón, I.; Barrera, J.; Hirata, G. A. Luminescence Properties and Cell Uptake Analysis of Y₂O₃:Eu, Bi Nanophosphors for Bio-Imaging Applications. *Journal of Materials Research and Technology* **2021**, *10*, 797–807.
- (34) Kunkel, N.; Goldner, P. Recent Advances in Rare Earth Doped Inorganic Crystalline Materials for Quantum Information Processing. *Zeitschrift für Anorganische und Allgemeine Chemie* **2018**, *644*, 66–76.

- (35) Zhong, T.; Goldner, P. Emerging Rare-Earth Doped Material Platforms for Quantum Nanophotonics. *Nanophotonics* **2019**, *8*, 2003–2015.
- (36) Fossati, A.; Liu, S.; Karlsson, J.; Ikesue, A.; Tallaire, A.; Ferrier, A.; Serrano, D.; Goldner, P. A Frequency-Multiplexed Coherent Electro-optic Memory in Rare Earth Doped Nanoparticles. *Nano Letters* **2020**, *20*, 7087–7093.
- (37) Anderson, R. B.; Smith, S. J.; May, P. S.; Berry, M. T. Revisiting the NIR-to-visible up-conversion mechanism in $\text{NaYF}_4:4\text{Yb}^{3+},\text{Er}^{3+}$. *Journal of Physical Chemistry Letters* **2014**, *5*, 36–42.
- (38) Berry, M. T.; May, P. S. Disputed Mechanism for NIR-to-Red Upconversion Luminescence in $\text{NaYF}_4:\text{Yb}^{3+},\text{Er}^{3+}$. *Journal of Physical Chemistry A* **2015**, *119*, 9805–9811.
- (39) Song, H.; Sun, B.; Wang, T.; Lu, S.; Yang, L.; Chen, B.; Wang, X.; Kong, X. Three-photon upconversion luminescence phenomenon for the green levels in $\text{Er}^{3+}/\text{Yb}^{3+}$ codoped cubic nanocrystalline yttria. *Solid State Communications* **2004**, *132*, 409–413.
- (40) Auzel, F. E. Materials and devices using double-pumped-phosphors with energy transfer. *Proceedings of the IEEE* **1973**, *61*, 758–786.
- (41) Sardar, D. K.; Nash, K. L.; Yow, R. M.; Gruber, J. B. Absorption intensities and emission cross section of intermanifold transition of Er^{3+} in $\text{Er}^{3+}:\text{Y}_2\text{O}_3$ nanocrystals. *Journal of Applied Physics* **2007**, *101*.
- (42) Yamada, N.; Shionoya, S.; Kushida, T. Phonon-assisted energy transfer between trivalent rare earth ions. *Journal of the Physical Society of Japan* **1972**, *32*, 1577–1586.
- (43) Liu, S.; Serrano, D.; Fossati, A.; Tallaire, A.; Ferrier, A.; Goldner, P. Controlled size reduction of rare earth doped nanoparticles for optical quantum technologies. *RSC advances* **2018**, *8*, 37098–37104.

- (44) de Oliveira Lima, K.; Rocha Gonçalves, R.; Giaume, D.; Ferrier, A.; Goldner, P. Influence of Defects on Sub-Å Optical Linewidths in $\text{Eu}^{3+}:\text{Y}_2\text{O}_3$ Particles. *Journal of Luminescence* **2015**, *168*, 276–282.
- (45) Peacock, R. D. *Rare Earths*; Springer, 2007; pp 83–122.
- (46) Chang, N.; Gruber, J. B.; Leavitt, R. P.; Morrison, C. A. Optical spectra, energy levels, and crystal-field analysis of tripositive rare earth ions in Y_2O_3 . I. Kramers ions in C_2 sites. *The Journal of Chemical Physics* **1982**, *76*, 3877–3889.
- (47) Gruber, J. B.; Leavitt, R. P.; Morrison, C. A.; Chang, N. Optical spectra, energy levels, and crystal-field analysis of tripositive rare-earth ions in Y_2O_3 . IV. C_{3i} sites. *The Journal of chemical physics* **1985**, *82*, 5373–5378.
- (48) Li, L.; Zhang, X.-Y.; Bai, Z.-H.; Dong, W.-L.; Shi, H.; Xue, Q.-X. Up-conversion and near infrared luminescence in Y_2O_3 : Er^{3+} , Yb^{3+} transparent ceramics. *Functional Materials Letters* **2016**, *09*, 1650011.
- (49) Capobianco, J. A.; Vetrone, F.; Boyer, J. C.; Speghini, A.; Bettinelli, M. Enhancement of red emission ($4\text{F}_9/2 \rightarrow 4\text{I}_{15/2}$) via upconversion in bulk and nanocrystalline cubic Y_2O_3 : Er^{3+} . *The Journal of Physical Chemistry B* **2002**, *106*, 1181–1187.
- (50) Zhang, L.; Pan, W.; Feng, J. Dependence of spectroscopic and thermal properties on concentration and temperature for $\text{Yb}^{3+}:\text{Y}_2\text{O}_3$ transparent ceramics. *Journal of the European Ceramic Society* **2015**, *35*, 2547–2554.
- (51) Kong, J.; Tang, D.; Lu, J.; Ueda, K. Spectral characteristics of a Yb^{3+} -doped Y_2O_3 ceramic laser. *Applied Physics B* **2004**, *79*, 449–455.
- (52) Auzel, F. Radiation trapping and self-quenching analysis in Yb^{3+} , Er^{3+} , and Ho^{3+} doped Y_2O_3 . *Optical Materials*. 2003; pp 103–109.

- (53) Wang, F.; Deng, R.; Wang, J.; Wang, Q.; Han, Y.; Zhu, H.; Chen, X.; Liu, X. Tuning upconversion through energy migration in core-shell nanoparticles. *Nature Materials* **2011**, *10*, 968–973.
- (54) Balaşa, I. G.; Arranz-Martinez, M. A.; Perrin, P.; Ngandeu Ngambou, M.; Hebbrecht, A.; Serrano, D.; Achard, J.; Tallaire, A.; Goldner, P. Rare Earth-Diamond Hybrid Structures for Optical Quantum Technologies.
- (55) Zhang, J.; Hao, Z.; Li, J.; Zhang, X.; Luo, Y.; Pan, G. Observation of efficient population of the red-emitting state from the green state by non-multiphonon relaxation in the $\text{Er}^{3+}\text{-Yb}^{3+}$ system. *Light: Science & Applications* **2015**, *4*, e239–e239.
- (56) Auzel, F. Upconversion and anti-stokes processes with f and d ions in solids. *Chemical reviews* **2004**, *104*, 139–174.
- (57) Wu, H.; Hao, Z.; Zhang, L.; Zhang, X.; Xiao, Y.; Pan, G.-H.; Wu, H.; Luo, Y.; Zhao, H.; Zhang, J. Phonon Energy Dependent Energy Transfer Upconversion for the Red Emission in the $\text{Er}^{3+}/\text{Yb}^{3+}$ System. *Journal of Physical Chemistry C* **2018**, *122*, 9611–9618.